Cellular/Molecular

Neuroendocrine Control of Synaptic Transmission by PHAC-1 in *C. elegans*

Aikaterini Stratigi,^{1*} Miguel Soler-García,^{1*} Mia Krout,² Shikha Shukla,¹ Mario De Bono,³ Janet E. Richmond,² and Patrick Laurent¹

¹Laboratory of Neurophysiology, ULB Institute for Neuroscience, Université Libre de Bruxelles, Brussels 1070, Belgium, ²Department of Biological Sciences, University of Illinois Chicago, Chicago, Illinois 60607, and ³Institute of Science and Technology, Klosterneuburg 3400, Austria

A dynamic interplay between fast synaptic signals and slower neuromodulatory signals controls the excitatory/inhibitory (E/I) balance within neuronal circuits. The mechanisms by which neuropeptide signaling is regulated to maintain E/I balance remain uncertain. We designed a genetic screen to isolate genes involved in the peptidergic maintenance of the E/I balance in the *C. elegans* motor circuit. This screen identified the *C. elegans* orthologs of the presynaptic phosphoprotein synapsin (snn-1) and the protein phosphatase 1 (PP1) regulatory subunit PHACTR1 (phac-1). We demonstrate that both phac-1 and snn-1 alter the motor behavior of *C. elegans*, and genetic interactions suggest that SNN-1 contributes to PP1-PHAC-1 holoenzyme signaling. De novo variants of human PHACTR1, associated with early-onset epilepsies [developmental and epileptic encephalopathy 70 (DEE70)], when expressed in *C. elegans* resulted in constitutive PP1-PHAC-1 holoenzyme activity. Unregulated PP1-PHAC-1 signaling alters the synapsin and actin cytoskeleton and increases neuropeptide release by cholinergic motor neurons, which secondarily affects the presynaptic vesicle cycle. Together, these results clarify the dominant mechanisms of action of the DEE70 alleles and suggest that altered neuropeptide release may alter E/I balance in DEE70.

Key words: developmental and epileptic encephalopathy-70; neuromodulation; neuropeptide; phactr1; synapsin; synaptic transmission

Significance Statement

Alterations of the excitatory/inhibitory (E/I) balance within neuronal circuits contribute to seizures. Early-onset epilepsies are associated with four variants of human PHACTR1 (called DEE70). In a genetic screen designed to isolate genes involved in the maintenance of the E/I balance by peptidergic neuromodulators, we identified the *C. elegans* orthologs of PHACTR1 and of synapsin. When introduced in *C. elegans*, the DEE70-associated variants reduced the E/I balance in motor circuits. Our results suggest that DEE70 variants induce the constitutive activity of an holophosphatase formed by PHACTR1. The constitutive holophosphatase signaling alters the synapsin and actin cytoskeleton and increases neuropeptide release, which secondarily decreases E/I balance in circuits.

Received Sept. 15, 2023; revised Dec. 9, 2024; accepted Dec. 17, 2024.

Author contributions: A.S., M.S.-G., M.K., M.D.B., J.E.R., and P.L. designed research; A.S., M.S.-G., M.K., S.S., and J.E.R. performed research; A.S., M.S.-G., M.K., S.S., J.E.R., and P.L. analyzed data; A.S., M.S.-G., and P.L. wrote the paper. P.L. is a research associate of the Belgian National Fund for Scientific Research (FRS-FNRS). K.S., M.S.-G., S.S., and P.L. are supported by grants from the FRS-FNRS. This work was supported by an Advanced ERC Grant (269058 ACMO) to M.D.B. We thank the team of Alexander Gottschalk for the snn-1(59A) strain. We thank the Imaging Facility of the Faculty of Medicine (LiMiF) of the Universite Libre de Bruxelles, supported by FRS-FNRS. This work made use of instruments in the Electron Microscopy Core of the University of Illinois Chicago Research Resources Center as well as the BioCryo facility of Northwestern University's NUANCE Center, which has received support from the SHyNE Resource (NSF ECCS-2025633), the IIN, and Northwestern's MRSEC program (NSF DMR-2308691). Some strains were provided by the CGC, which is funded by NIH Office of Research Infrastructure Programs (P40 00010440).

*A.S. and M.S.-G. contributed equally to this work.

The authors declare no competing financial interests.

S.S.'s present address: Buck Institute for Research on Aging, Novato, California.

Correspondence should be addressed to Patrick Laurent at patrick.laurent@ulb.be.

https://doi.org/10.1523/JNEUROSCI.1767-23.2024

Copyright © 2025 the authors

Introduction

Neuromodulation by neuropeptides contributes to circuit adaptability, stability, and the integration of contextual information by changing the cellular and synaptic properties of target neurons (Bargmann, 2012; Marder, 2012). Neuropeptides also play a significant role in preserving the balance between excitatory and inhibitory signals within circuits (E/I balance). This homeostatic function of neuropeptides contributes to both fear learning and prevention of pathological disorders such as epilepsy and autism (Nelson and Valakh, 2015; Agostinho et al., 2019; Hornberg et al., 2020; Melzer et al., 2021).

The sinusoidal locomotion of *C. elegans* results from coordinated muscle contraction–relaxation mediated by a set of interconnected cholinergic and GABAergic motor neurons

(White et al., 1976, 1986). Mutations producing abnormal activities in the motor circuit can cause aberrant muscle contractions and uncoordinated locomotion (Brenner, 1974). Decades of studies have revealed multilevel regulation of the E/I balance in the motor circuit of *C. elegans*, including regulation by peptidergic inputs. For example, increased production and secretion of the FMRF-like peptide FLP-18 inhibits epileptic-like convulsions caused by unbalanced E/I in the locomotor circuit of *acr-2(gf)*, a gain of function mutation in the neuronal ionotropic acetylcholine (ACh) receptor ACR-2 (Stawicki et al., 2013; McCulloch et al., 2020).

The mechanisms of homeostatic control of E/I balance in circuits by neuropeptides remain poorly understood. Here, we designed a genetic screen aimed at understanding how neuropeptide/FLP-18 signaling regulates the E/I balance of the C. elegans motor circuit. Among the FLP-18 signaling effectors, we isolated the single *C. elegans* ortholog of synapsins (*snn-1*) and PHACTR1 (phac-1). Synapsins are presynaptic phosphoproteins controlling synaptic vesicle (SV) and dense core vesicle (DCV) dynamics (Cesca et al., 2010). In humans, four proteins called the PHosphatase 1 and ACTin Regulators (PHACTR1-4) are protein phosphatase 1 (PP1) family regulatory subunits (Allen et al., 2004). The binding of PP1 to human PHACTR1 improves the specificity of the PP1-PHACTR1 holophosphatase for its substrates, which include structural and regulatory cytoskeletal proteins (Fedoryshchak et al., 2020). Accordingly, PHACTR1 signaling has been shown to remodel the actin cytoskeleton in a melanoma cell line (Wiezlak et al., 2012). PHACTRs are highly expressed in the nervous system, but their function remains unclear (Allen et al., 2004). De novo variants in PHACTR1 are associated with developmental and epileptic encephalopathy 70 (DEE70; Hamada et al., 2018; Marakhonov et al., 2021). DEEs are severe forms of early-onset epilepsy caused by rare—often de novo-mutations in genes involved in neuronal proliferation, migration, excitability, synaptic transmission, and plasticity (McTague et al., 2016; Guerrini et al., 2023). Knockdown in mice suggests that PHACTR1 controls neuronal migration and dendritic tree complexity (Hamada et al., 2018).

Here, we demonstrate that PHACTR1/PHAC-1 and synapsin/SNN-1 contribute to the E/I balance within the *C. elegans* motor circuit. PHAC-1 signaling increases DCV secretion of neuropeptides from motor neurons, which secondarily affects neuromuscular junction (NMJ) signaling. Introducing three pathological PHACTR1 point mutations associated with DEE70 into the *C. elegans phac-1* gene generates a constitutively active PP1-PHAC-1 holophosphatase that disturbs the E/I balance of the motor circuit demonstrating a conserved neuromodulatory role.

Materials and Methods

Strains. Strain maintenance and genetic manipulation were performed as previously described (Brenner, 1974). Animals were cultivated at room temperature on nematode growth medium (NGM) agar plates seeded with OP50 bacteria. On the day before experiments, L4 larval stage animals were transferred to fresh plates seeded with OP50 bacteria. The strains generated or obtained, as well as the primers used for genotyping, are provided in Extended Data 1.

Constructs, transgenes, and germline transformation. C. elegans N2 genomic DNA or cDNA was used as template for cloning PCRs. Cloning PCRs were performed using Phusion High-Fidelity DNA polymerase (M0530L, New England Biolabs) and then validated by Sanger sequencing. Details on primer used are provided in Extended Data 1. Expression plasmids used to generate transgenic animals were generated by means of Multisite Three-Fragment Gateway Cloning (Invitrogen, Thermo Fisher Scientific). To generate the PHAC-1(2R/A) plasmid, site-

specific mutagenesis was performed by standard PCR using a plasmid containing wild-type *phac-1* cDNA sequence as template. Primers used are provided in Extended Data 1. Details on expression plasmids are provided in Extended Data 1. All transgenic worms were generated by microinjection using standard techniques (Mello et al., 1991). For most injected constructs, injection mixes were composed of 30 ng/µl targeting constructs, 30 ng/µl of coinjection markers, and 40 ng/µl of 1 kb Plus DNA mass ladder (Invitrogen, Thermo Fisher Scientific) as carrier DNA, for a final injection mix DNA concentration of 100 ng/µl.

Gene editing. Gene editing by CRISPR Cas-9 was done by direct injection of Cas9 guide-RNA ribonucleoprotein complexes into the syncytial gonad as previously described (Ghanta and Mello, 2020). CRISPR-mediated homologous recombination with a DNA repair template is increased by mixing, melting, and reannealing template dsDNA. An injection mix was prepared with 30 pmol of Cas9, 90 pmol of tracrRNA, 95 pmol crRNA, 500 ng melted dsDNA, and 800 ng myo-2p::RFP plasmid. For *phac-1* gene editing, ~20 injected P0 animals were cultured individually. We selected three P0 plates with ~40% of the progeny carrying the myo-2p::RFP transgene to pick F1. We singled 24 F1 for point mutants and 48 for wrmScarlet (wSc) insertion. *phac-1* gene editing was screened using PCR-restriction digest. The gRNA and repair template used are provided in Extended Data 1.

RNAi knockdown of Ex[phac-1::SL2-tagRFP]. Worms were raised on NGM plates containing IPTG and seeded with the E. coli HT115(DE3) strain transformed with the plasmid L4440 containing RNAi against F26H9.2/phac-1, against dpy-11 (as positive control), or against the empty vector as negative control. The F26H9.2 RNAi strain carries a 1,194 bp PCR fragment between primers ATCACGACGGGCTAC TTTTG and CGGATCAGCGTAAATTTGAA. As IPTG is light sensitive, these strains were grown in the dark under otherwise normal conditions. Imaging was performed as described below.

Morphological and behavioral video recording. Video recordings were acquired at 15 frames per second (fps) with three array cameras connected to a computer equipped with Motif software (Loopbio).

Worms were segmented, tracked, and skeletonized using Tierpsy Tracker (Javer et al., 2018), freely available on https://github.com/ Tierpsy. After analysis, the features of interest were extracted. For locomotion assays, 30 worms were placed on low peptone NGM with OP50 seeded $\sim\!\!16$ h before. Each genotype was recorded three times. Worms were allowed to adapt to 7% O_2 for 5 min before video recording started. Worms were recorded for 5 min once the gas mixture pumped into the chamber was changed from 7 to 1% O_2 . Midbody forward speed parameter was extracted from the videos and compared across the different genotypes.

Isolation of flp-18(XS) suppressors and identification. flp-18(XS) suppressors were identified in a forward genetic screen. Animals from the strain OQ60 (Is[pflp-18::flp-18-SL2-GFP; ccGFP] V; Extended Data 1) carrying stably integrated flp-18(XS) were mutagenized with EMS using standard procedures, and 8-12 P0 animals were isolated on eight P0 plates (Brenner, 1974). Subsequently, 4-6 F1 animals from each P0 plate were placed on 15 NGM growth plates, and their F2 progeny were examined for locomotion. Forty-eight F2 mutants were isolated in which locomotion appeared restored, and worms from their F3 plates were scored. Coordination score: we blindly scored from −1 to 4 (0 being unchanged and 4 being like N2) the following parameters typical of the flp-18(XS) strain-slow locomotion on food, and off food, deep body curvature during forward locomotion, frequent reversals, abnormally long reversals when prodded, and long reversals with extreme curvature when prodded. The scores were combined, and as the flp-18(XS) control was slightly off 0, we normalized the values to N2. Genomic DNA was isolated from the 25 best suppressor strains identified in the forward genetic screen. The Genomics core facility of Universite Libre de Bruxelles performed paired-end 150 bp sequencing on Illumina MiSeq; 20× coverage. Sequences were aligned to the original OQ60 and N2 strains. All high score mutations within ORFs were highlighted, and candidate suppressors were ranked according to repeated observations within the 25 strains

sequenced. We observed three mutations for npr-5, three mutations for cmk-1, two mutations for crh-1, and two mutations for ric-19. Deletion appeared only once in snn-1 and phac-1. The ulb03 and ulb14 alleles were crossed to the polymorphic Hawaiian CB4856 strain. Approximately 60 F2 progeny of this cross all exhibiting GFP expression from the flp-18(XS) integrated construct but displaying improved locomotion (homozygous mutants for suppressor) were identified using a compound fluorescence microscope. Genomic DNA was isolated from their pooled progeny and subjected to sequencing. The density of unique and polymorphic single nucleotide polymorphisms was assessed using online tools (CloudMap) on the usegalaxy.org server as previously described (Minevich et al., 2012). The generated chromosomal level frequency plots for parental alleles showed a peak of unique variants on chromosome 1 for ulb03 and 4 for ulb14. Within the middle of these peaks, deletion mutations were identified for phac-1 (ulb03) and snn-1(ulb-14). The alleles were outcrossed twice in N2 (CGC) before further analysis.

Aldicarb paralysis assay. Aliquots of stock aldicarb [33386-Sigma, 100 mM in 70% (v/v) ethanol] were kept at 4°C until its use. Aldicarb plates (0.5, 1, or 2 mM in low peptone NGM) were prepared at least 3 d before the experiments. Figure to figure variability in paralysis dynamics reflects variability in aldicarb concentration from stock and/ or in batches of plates. For all aldicarb assays, we measured the time course for paralysis of 20-25 animals in the presence of aldicarb. For each replicate, a curve was interpolated via nonlinear regression [Sigmoidal, 4PL; X is time; GraphPad (8.4) Prism], and the time point at which 50% of animals are paralyzed was calculated [which we called half-maximum response (HMRT)]. All replicates are visible in scatterplots; 3-16 independent replicates correspond altogether to 60-320 animals assayed. As much as possible, all replicates of each figure were collected with a single batch of plates, for all genotypes. L4 worms were picked 20 h before the assay. One hour before the assay, 10 µl of OP50 was placed carefully on each aldicarb plate to maintain the population of animals in the center of the plate. Animals were placed on the bacterial lawn, and paralysis of each worm was tested every 30 min. The criterion for paralysis was the absence of midbody movement after poking three times with our worm picker. Paralyzed worms were removed from the plates and recorded. For each strain, the experiments were performed 3-16 times with 20-30 animals per replicate. The presented data are the mean paralysis HMRT ± SEM. All assays included the N2 control strain.

Levamisole assays. Levamisole aliquots (L0380000-Merck) were freshly prepared before the assay. The assays were performed essentially as described (Senti and Swoboda, 2008). Briefly, low peptone NGM agar plates supplemented with levamisole at concentrations ranging from 0.2 to 0.8 mM were prepared. L4 larvae were isolated 20 h before the assay. For each plate, worms were placed onto the levamisole plates and inspected for induced paralysis every 10 min. Each plate corresponds to 20–25 adult worms, we made three replicates for each genotype, and the experiment was performed three times. Worms were considered paralyzed when they did not respond to three consecutive prodding with the platinum wire pick.

Heat-shock expression of phac-1(gf). Strains were grown at 15°C to minimize leaky expression from the hsp-16.41 promoter. To heat-shock animals, NGM plates were wrapped with parafilm and immersed in a 34°C water bath for 30 min. The aldicarb assay was performed as described 16 h later. The expression of the PHAC-1(2R/A) protein was confirmed by observing the expression of the red fluorescence tag and was present throughout the assay.

Generation of (phosphoS9)-SNN-1 antibody and Western blot. The antibody against phosphorylated SNN-1 was raised against the peptide sequence FKRKF-S(PO3H2)-FSEDEG with KLH carrier protein by Eurogentec. Western blotting was performed as described in Haque et al. (2020). Worms were washed thrice with M9 buffer and resuspended in phosphate-buffered saline (PBS). These worms were sonicated in PBS containing a protease inhibitor cocktail and a phosphatase inhibitor.

Sonication was performed at 25 amplitudes for 3 min with a pulse time of 15 s. The sonicated lysate was centrifuged at $16,000 \times g$ for 30 min at 4°C to remove debris, and supernatant containing the total protein was kept. 30 µg of total protein was loaded in 10% sodium dodecyl sulfate polyacrylamide gel electrophoresis. The primary antibodies used for Western blot were anti-phosphorylated SNN-1 (1:1,000) and anti-histone H3 antibody (1:1,000). Chemiluminescence was detected using LAS 3000 GE ImageQuent, and densitometric analysis was performed by ImageJ software (ImageJ, National Institutes of Health).

Fluorescence imaging. Worms were synchronized either by bleaching a population of gravid adults or using an egg-laying window. Worms were reared at 20°C and imaged at the L4 stage unless otherwise stated. Worms were mounted on 2% agarose pads diluted in M9 solution, placing them in a droplet of M9 on the agar pad, and then covered with a coverslip. Animals were immobilized with 10 mM levamisole (L9756-Sigma) diluted in the agar pad and in the M9 droplets. Levamisole agar pads and M9 dilutions were freshly made for each strain. Levamisole is a nicotinic ACh muscle receptor agonist that induces paralysis after $\sim\!10$ min.

Images were acquired at the Light Microscopy Facility LiMiF (http:// limif.ulb.ac.be) on a LSM780NLO confocal system fitted on an Observer Z1 inverted microscope (Carl Zeiss). Images were acquired using a LD C Apochromat 40×/1.1 W Korr M27 objective or an alpha Plan Apochromat 63×/1.46 Oil Korr M27 objective. The settings were as follows: the frame size was set at 1,024 × 1,024 pixels with a pixel size of $0.13~\mu\text{m}\times0.13~\mu\text{m},$ the pinhole size was set to 1 Airy Unit, and Z-step optical sections were acquired at 0.4 µm steps. For individual channel acquisitions, the main beam splitter matched the excitation wavelength of each used fluorophore. The following fluorophore excitation (Ex) and detection wavelength (DW) were used: mEGFP/NG (Ex, 488 nm; DW, 493-569 nm), Venus (Ex, 514; DW, 517-588), and wSc/TagRFP (Ex, 543 nm; DW, 570-695 nm). Fluorophore Ex and DW ranges were set according to the information available at the FPbase database for each fluorophore (Lambert, 2019). Laser power and detector gain settings were adjusted to maximize signal-to-noise ratio and minimize saturation. Images were saved in .czi Zeiss file format. For examination of different genetic backgrounds, each strain was imaged on at least two independent days (always including control N2 and tested mutants), and the data were pooled together. Acquisition settings were the same across session and genotypes per presynaptic marker for quantitative analysis.

Image processing. Confocal images were processed using FIJI (Schindelin et al., 2012) and Zen 2.6 Pro (Blue edition) software (Carl Zeiss). Z-stack acquisitions were converted into a 2D image using maximum intensity projections to obtain a flattened image representative of the 3D volume. For fluorescence along the DA axon, we imaged a 100 μ m \times 3 μ m area along the dorsal cord right after the posterior pharynx bulb and corresponding mostly to the DA1 axon. A Z-stack was obtained for each worm at 0.4 µm steps. A line was traced along the axon signal to collect fluorescence intensity along the axon. The same line was slightly shifted away from the axon to collect background fluorescence. Fluorescence intensity along the axon minus background fluorescence was analyzed using custom software written in IGOR Pro (WaveMetrics), as described previously (Laurent et al., 2018). Peak fluorescence was detected if 2× brighter than the median plus 20% standard deviation, and the width was >0.3, <10 µm at half-maximum. These bright puncta corresponded to the local accumulation of the marker and were further analyzed to extract their fluorescence intensity and puncta density per 10 µm.

Fluorescence recovery after photobleaching (FRAP) assay. For the FRAP experiments, animals were anesthetized in 5% agarose to prevent moving over a longer time. An alpha Plan Apochromat $63\times/1.46$ Oil Korr M27 objective was used to focus the dorsal cord. A rectangular region of $12.1~\mu m \times 3.1~\mu m$ containing part of the cord was selected, where bleaching of Venus was performed using 488 nm laser at 60% power. A total of 120 frames were taken at 0.5 frames/second, with three

frames taken before bleaching. Normalization of the data was performed using the easyFRAP software (https://easyfrap.vmnet.upatras.gr/) as described in Giakoumakis et al. (2017). To account for acquisition bleaching, a nonphotobleached region of the dorsal cord was selected as control. Background fluorescence was measured and subtracted from both control and photobleached regions. After normalization, standard curve fitting techniques allow the calculation of the mobile fraction.

Electrophysiology. Worms were immobilized on a Sylgard-coated coverslip using Histoacryl Blue glue, and a lateral cuticle incision was made with a glass needle, exposing the ventral medial body wall muscles. Nematodes were viewed during recordings using a 40× water immersion objective on a Zeiss Axioskop. Body wall muscle recordings were made in the whole-cell voltage-clamp configuration (holding potential, -60 mV) using an EPC-10 patch-clamp amplifier (HEKA) and digitized at 1 kHz. Voltage-clamp recordings were typically maintained for 2-5 min. Voltage clamping and data acquisition were controlled by Pulse software (HEKA) run on a Dell computer. Modified Ascaris Ringer contained the following (in mM): 150 NaCl, 5 KCl, 5 CaCl₂, 4 MgCl₂, 10 glucose, 5 sucrose, and 15 HEPES, pH 7.3, ~340 mOs. Fire-polished recording pipettes with resistances ranging from 5 to 9 $M\Omega$ were pulled from borosilicate glass (World Precision Instruments). The patch pipette was filled with the following (in mM): 120 KCl, 20 KOH, 4 MgCl₂, 5 (N-tris[hydroxymethyl] methyl-2-aminoethane-sulfonic acid), 0.25 CaCl₂, 4 Na₂ATP, 36 sucrose, and 5 EGTA, pH 7.2, ~315 mOsm. ACh and GABA minis were pharmacologically separated by perfusing d-tubocurarine (dTBC; 10-4 M) during recordings, to isolate the GABA minis. Data were acquired using Pulse and Patchmaster software (HEKA). Subsequent analysis and graphing were performed using Pulsefit (HEKA), Mini analysis (Synaptosoft), and IGOR Pro (WaveMetrics). Stimulus-evoked EPSCs were generated by placing a borosilicate pipette on the ventral nerve cord (VNC; one muscle distance from the recording pipette) and applying a 0.2 ms, 20 V square pulse using a stimulus current generator (WPI).

Electron microscopy. The worm strains were prepared using highpressure freeze fixation and freeze substitution as previously described (Weimer et al., 2006; Liu et al., 2021). Briefly, 20-30 young adult worms were placed in specimen chambers filled with E. coli and frozen at -180° C, using liquid nitrogen under high pressure (Leica HPM 100). After freezing, samples underwent freeze substitution (Reichert AFS, Leica) using the following program: -90°C for 107 h with 0.1% tannic acid followed by 2% OsO4 in anhydrous acetone, incrementally warmed at a rate of 5°C/h to -20°C, and kept at -20°C for 14 h before increasing the temperature by 10°C/h to 20°C; samples were then infiltrated with 50% Epon/acetone for 4 h, 90% Epon/acetone for 18 h, and 100% Epon for 5 h; finally, samples were embedded in Epon and incubated for 48 h at 60°C (Liu et al., 2021). Ultrathin (40 nm) serial sections were acquired using an Ultracut 6 (Leica) and collected on formvar-covered, carboncoated copper grids (EMS, FCF2010-Cu). Sections were poststained with 2.5% aqueous uranyl acetate for 4 min, followed by Reynolds lead citrate for 2 min (Liu et al., 2021). Images were obtained using a JEOL JEM-1400F transmission electron microscope, operating at 80 kV. Micrographs were acquired using a BioSprint 12M-B CCD Camera with AMT software (Version 7.01). Cholinergic synapses at the NMJ of the VNC were identified based on established synaptic morphology (White et al., 1986). The DP of cholinergic synapses typically orient at an acute angle of 30–45° to the muscle, and the synapses are often dyadic. These can be distinguished from GABAergic synapses, which are larger than their cholinergic motor neuron counterparts, and the active zones in these synapses form a direct, perpendicular angle with muscle arms. Sections containing a DP, as well as two flanking sections on either side of the DP, were aligned and analyzed blinded to genotype using TrakEM2 and ROI features of NIH FIJI/ImageJ software, respectively (Cardona et al., 2012; Schindelin et al., 2012). The aligned stacks were imported into 3Dmod/IMOD (University of Colorado; https://bio3d. colorado.edu/imod/) to create a 3D model of reconstructed individual synapses. SVs were counted as docked when the vesicle membrane was fully contacting the plasma membrane of the neuron terminal (distance, 0 nm); vesicles that were within 1–5 nm of the plasma membrane that exhibited small tethers were not scored as docked. The distribution of docked vesicles from the DP was calculated for each section containing a DP, as well as one section on either side, using the ROI data from FIJI with MATLAB scripts written by Watanabe and Jorgensen Laboratories (Watanabe et al., 2020). Values were imported to Prism (GraphPad) for graphing and statistical analysis using one-way ANOVA with Tukey's post hoc analysis, or Kruskal–Wallis with Dunn's test, for multiple comparisons.

Raw data and statistical analysis. Raw data and statistical analysis used are available in Extended Data 2. Statistical tests are summarized in figure legends. GraphPad Prism 8.4 was used to perform statistical tests and calculate p- or q-values.

Results

A suppressor screen highlights the involvement of *snn-1* and *phac-1* in the neuromodulation of NMJs

The transcriptional regulation of FLP-18 signaling contributes to the tuning of E/I balance in the worm locomotory circuit (Stawicki et al., 2013; McCulloch et al., 2020). We and others observed that overexpression of the FLP-18 neuropeptide under its promoter alters the locomotion of *C. elegans*: animals reverse more frequently, and body bends are deeper during forward locomotion and extremely deep during reversals, leading to slower and uncoordinated locomotion on agarose plates and reduced thrashing frequency in liquid (Cohen et al., 2009; Stawicki et al., 2013; Florman and Alkema, 2022; Fig. 1a,b). FLP-18 receptors are expressed on sensory neurons, motor neurons, and muscles (Cohen et al., 2009; Bhardwaj et al., 2018). We thought that the FLP-18-induced behavior may report neuropeptide regulation of the motor circuit E/I balance. We first validated this model by crossing the FLP-18 overexpressing strain (flp-18(XS)) with 27 mutants defective in genes controlling neuropeptide expression, DCV biogenesis, peptide release, or GPCR signaling. As expected, these mutants modulated the FLP-18-induced uncoordinated locomotion on plates (Fig. 1c). Specifically, mutants that reduce peptidergic signaling (Fig. 1c, d, green) improved coordination of locomotion on the agar plate, whereas mutants that enhance peptide signaling (Fig. 1c,d, red) exacerbated the flp-18(XS) phenotype. Mutants with the most prominent effects also impacted thrashing frequency in liquid (Fig. 1e,f). The strongest suppression was observed for npr-5, which encodes a FLP-18 receptor expressed in sensory neurons, motor neurons, and body wall muscles (Cohen et al., 2009; Stawicki et al., 2013; Florman and Alkema, 2022). We leveraged the FLP-18-induced behavior to perform a suppressor screen aimed at identifying genes involved in neuropeptide regulation of the motor circuit E/I balance. We mutagenized the FLP-18 overexpressing strain and isolated 25 strains that exhibited improved locomotion despite the overexpression of FLP-18. We identified some of the causal variants by whole-genome sequencing and confirmation by crossing FLP-18(XS) with other available alleles. These include npr-5(ulb08), crh-1(ulb06), cmk-1(ulb07), ric-19(ulb12), snn-1(ulb14), and phac-1(ulb03) (Fig. 1c, blue). Transcriptional regulation of flp-18 by crh-1 was previously reported (Bhardwaj et al., 2018). Our flp-18 overexpression strain coexpressed GFP in an operon with flp-18. As expected the CREB transcription factor mutant crh-1(ulb06) and the CAMKI mutant *cmk-1(ulb07)* reduced GFP expression from the *flp-18* promoter. Mutations in *ric-19*, the ortholog of islet cell autoantigen (ICA69), were previously observed to reduce DCV biogenesis (Sumakovic et al., 2009). Therefore, crh-1, cmk-1, and ric-19 likely act in the FLP-18 expressing neurons

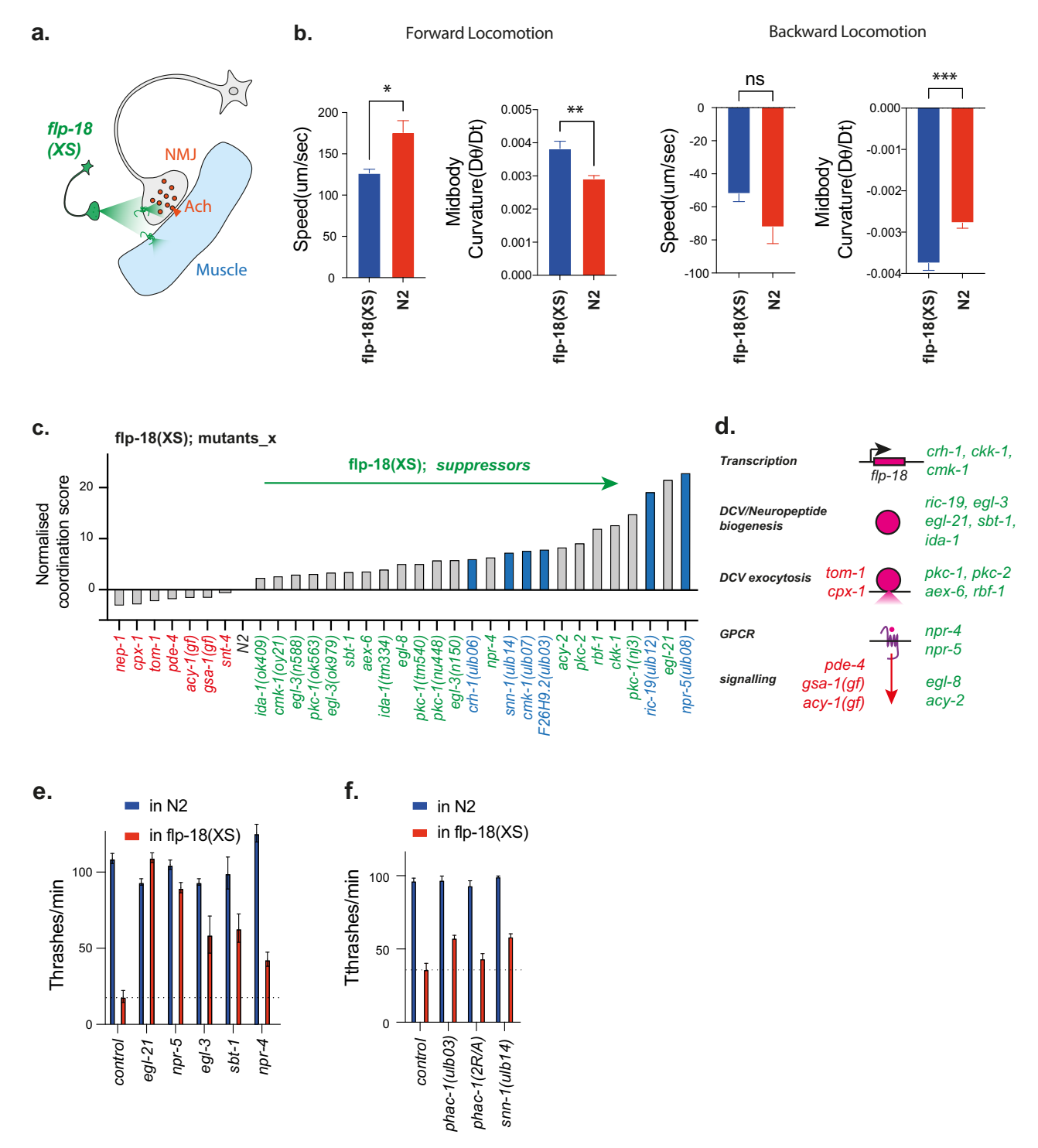


Figure 1. A suppressor screen allows the identification of genes involved in neuromodulation by FLP-18. a, Overexpression of the neuropeptide FLP-18 under its own promoter (flp-18(XS)) alters the locomotion of C. elegans through modulation of the NMJ. b, Placed at 1% 0_2 , the average speed of forward locomotion is reduced in flp-18(XS) compared with N2, while the average midbody curvature is increased in flp-18(XS) compared with N2; N = 90 individuals. Data are plotted as the mean \pm SEM. Statistics: t test. ns, p > 0.05; **, $p \le 0.05$; **, $p \le 0.01$; ***, $p \le 0.001$. c, This locomotion phenotype was used in a suppressor screen to identify genes reducing neuropeptide signaling at the NMJ. A coordination score was determined blindly for each strain carrying FLP-18(XS) (compared with the locomotion of the FLP-18(XS) in the N2 background strain, 0 is unchanged, > 20 is fully rescued, negative values are for worsened locomotion; see Materials and Methods). Strains isolated from the FLP-18 suppressor screen are highlighted in blue; the causal genes identified include npr-5, cth-1, cth-1, ric-19, snn-1, and F16H9.2/phac-1; the control genes crossed with FLP-18(XS) are highlighted in red and green. d, Control genes were selected across genes promoting (in green) or inhibiting (in red) neuropeptide transcription and biogenesis, DCV exocytosis, and neuropeptide signaling at the NMJ. e, To quantify locomotion, the frequency of thrashes in liquid was measured for each mutant in the N2 genetic background (in blue) and in the flp-18(XS) background (in red); N = 30. The frequency of thrashes is strongly reduced by FLP-18 overexpression. The strongest suppressors of the flp-18(XS) thrashing phenotype are egl-21 and npr-5. f, The frequency of thrashes in liquid for a subset of suppressor mutants identified in the forward genetic screen; N = 30. phac-1(ulb03) and snn-1(ulb14) partially suppress the flp-18(XS) thrashing phenotype, but not phac-1(2R/A

to promote neuropeptide signaling (Fig. 1*d*). Among the other suppressors identified and confirmed by the thrashing assay, we identified a deletion in the single *C. elegans* ortholog of synapsin, *snn-1(ulb14)* (Fig. 1*f*). Synapsins are phosphoproteins that tether SVs to each other, forming SV clusters (Cesca et al., 2010). We also identified a deletion allele in *F26H9.2(ulb03)*, corresponding to the single *C. elegans* ortholog of the four mammalian PHosphatase and ACtin Regulators (PHACTRs; Fig. 1*f*).

The C-terminal domains of mammalian PHACTRs include three RPEL motifs (involved in G-actin binding: Pfam PF02755) and one PP1c binding domain. These elements are well conserved in F26H9.2, while the unstructured N-terminal region is poorly conserved (Fig. 2a,b). Based on this homology, we renamed F26H9.2 as PHACTR: phac-1. The phac-1(ulb03) allele obtained from the screen corresponded to a C-terminal deletion and frameshift removing RPEL motifs and the PP1 binding domain. We obtained two other likely null alleles of phac-1 from the Japanese C. elegans consortium that corresponds to large C-terminal deletions, phac-1(tm2463) and phac-1(tm2453), the latter also possessing an early stop codon (Fig. 2a, orange). Under normal cultivation conditions, the phac-1 deletion mutants grew and developed as well as wild-type controls (N2).

phac-1 is expressed broadly including in the nervous system

To determine the expression pattern of *phac-1*, we generated a knock-in strain with wSc fused to the C-terminus of PHAC-1. In this reporter strain, wSc exhibited weak but widespread expression. We could identify expression in pharyngeal muscles, head muscles, excretory cells, and unidentified neurons that project to the nerve ring (NR; Fig. 3a). To better observe expression patterns, we generated an overexpression reporter strain in which 3 kb of the phac-1 endogenous promoter sequence drive the expression of *phac-1* along with TagRFP in an SL2 operon. TagRFP expression was observed from the early embryo to the adult stage (Fig. 3b). The TagRFP expression pattern appeared like the knock-in strain, including strong expression in

pharyngeal muscles, head muscle cells, excretory gland and canal cells, phasmid and amphid socket glia, and neurons projecting to the NR (Fig. 3c). To further refine the neuronal expression pattern, this strain was treated with RNAi to knock down TagRFP in non-neuronal tissues (Schenk et al., 2010). As neurons are relatively resistant to RNAi knockdown, we could observe expression of TagRFP in both cholinergic and GABAergic motor neurons of the VNC as well as in ALM, CAN, and HSN, among other neuron types (Fig. 3d–g). N- and C-terminal GFP fusion constructs localized to the cytoplasm and neurites, but not to the nucleus (Fig. 3h).

phac-1 regulates cholinergic NMJ signaling

ACR-2 is a subunit of a nicotinic receptor expressed in *C. elegans* cholinergic motor neurons, and acr-2(gf) causes cholinergic overexcitation accompanied by reduced GABAergic inhibition in the locomotor circuit. Neuroendocrine regulation of the motor circuit by neuropeptides, including FLP-18, has been shown to modulate the spontaneous convulsions observed in the *acr-2(gf)* strain (Stawicki et al., 2013). To test the potential role of phac-1(tm2453) in the neuroendocrinal control of the motor circuit E/I balance, we crossed phac-1 mutants into the acr-2(gf) strain. We observed that phac-1(tm2453) reduced the convulsions induced by the *acr-2(gf)* allele (Fig. 4*a*; p = 0.0235). phac-1(tm2453) also improved the slow locomotion (Fig. 4b; p < 0.0001) and the hypercontracted phenotype associated with the acr-2(gf) mutation (Fig. 4c; p = 0.0045). In the absence of acr-2(gf), the locomotion speed of phac-1(tm2453) was reduced compared with N2 (Fig. 4d; p < 0.0001).

Suppressors of *acr-2(gf)*-induced convulsions include genes involved in neurotransmitter or neuropeptide release (McCulloch et al., 2020). To support an alteration of the NMJ signaling in *phac-1* deletion mutants, we used the aldicarb-induced paralysis assay. Application of the acetylcholinesterase inhibitor aldicarb prevents ACh hydrolysis. The resulting accumulation of ACh at NMJs causes hypercontracted paralysis within hours. Resistance

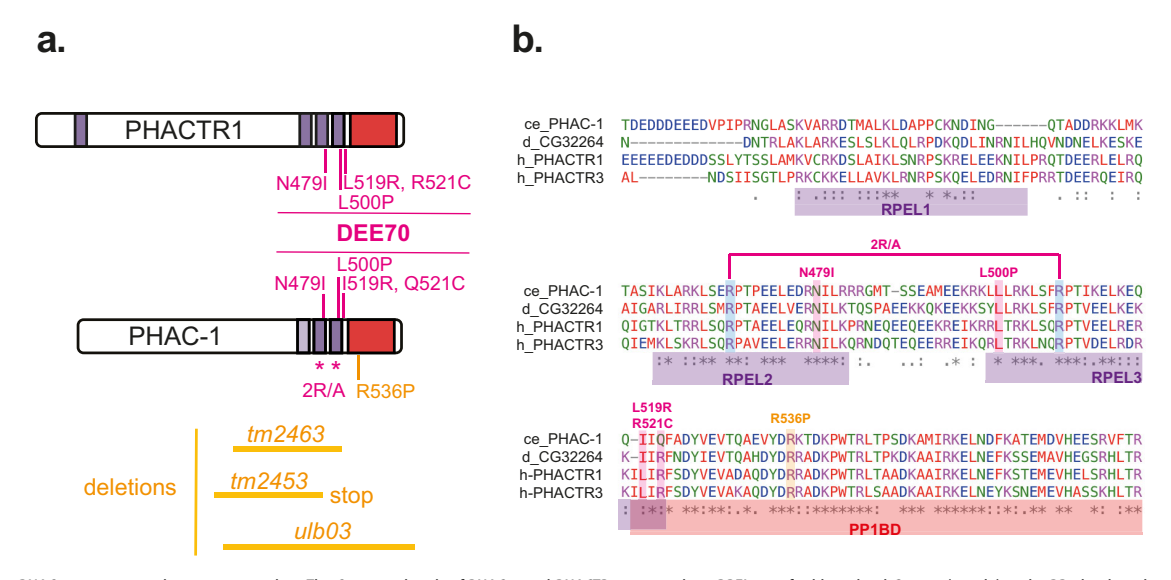
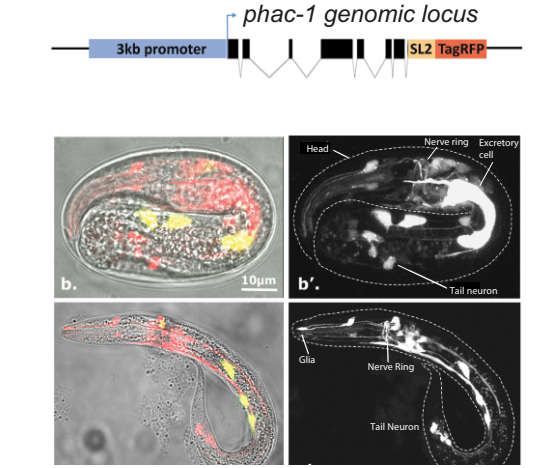


Figure 2. PHAC-1 structure and mutations used. **a**, The C-terminal ends of PHAC-1 and PHACTRs contain three RPEL motifs able to bind G-actin (purple) and a PP1 binding domain (red). The alleles of *phac-1* obtained by random mutagenesis or obtained by CRISPR-Cas9 approaches are indicated. Deletion alleles and R536P substitution are indicated in orange and cause null and hypomorph mutants, respectively. gf alleles are indicated in magenta including the variants of PHACTR1 associated with DEE70. **b**, Alignment of the C-terminal sequence of PHAC-1 with the *Drosophila melanogaster* ortholog, CG32264, and the human orthologs PHACTR1 and PHACTR3. The three RPEL motifs are underscored in purple, and the PP1-binding domain (PP1BD) is underscored in red; notice the overlap between the last RPEL motif and the PP1 binding domain. The alignment shows a high degree of conservation in the last two RPEL motifs and the PP1BD, including the amino acids associated with human DEE70. The 2R/A and DEE70-associated mutations are indicated in magenta and R536P in orange.

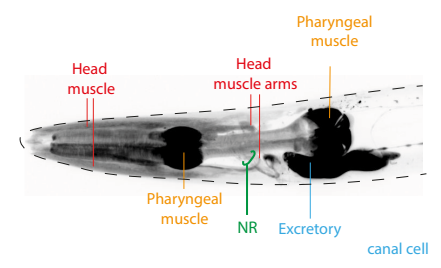
a. phac-1-wrmScarlet knockin

Pharyngeal muscle Nerve Ring Pharyngeal muscle Nerve ring

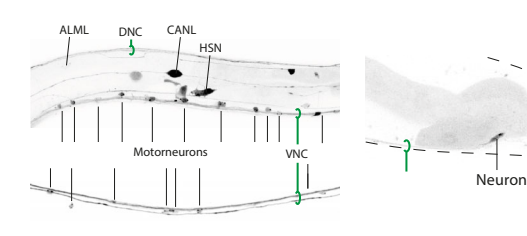
b. Ex[phac-1-SL2tagRFP] overexpression



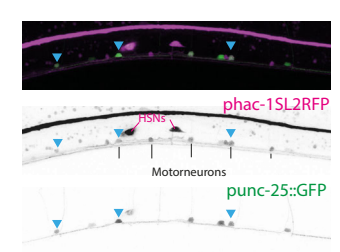
c. Ex[phac-1SL2tagRFP]



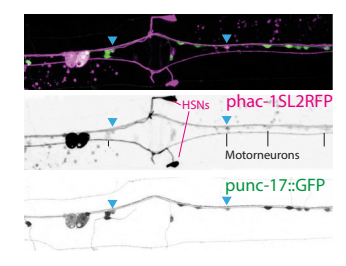
d. Ex[phac-1SL2tagRFP]



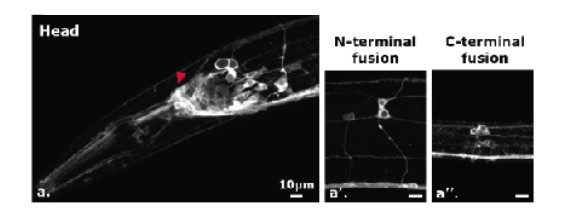
f. GABAergic motorneurons



g. Cholinergic motorneurons



h. Ex[prab-3::phac-1 N- and C-ter GFP fusions]



e. Ex[phac-1SL2tagRFP]

Ex[prab-3::GFP-PP1-phac-1]

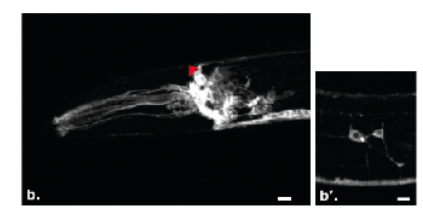


Figure 3. PHAC-1 is expressed broadly, including in cholinergic and GABAergic neurons of the VNC. *a*, Expression in D1 adults of wSc in a CRISPR knock-in reporter strain carrying *wSc* C-terminally fused to the *phac-1* ORF. Expression of wSc is weakly observed in the pharyngeal muscles, head muscles, excretory cells, and the NR. *b*, A second reporter strain carries an extrachromosomal array, where SL2-TagRFP forms an operon regulated by a 3 kb promoter and a 3 kb fragment of the *phac-1* locus including a large intron. Representative images of TagRFP expression at embryonic (top) and L1 (bottom) stages. Expression of TagRFP (red in b and grayscale in b') is widespread, including expression in neurons and glial cells and in excretory glands, cells, and canals. The coelomocyte's coinjection marker is observed in green. *c-g*, The adult expression pattern of TagRFP was determined in a reporter strain carrying *Ex[phac-1-SL2TagRFP]*. *c*, In the head, expression is observed in the pharynx, muscle, excretory cells, and NR. *d*, In the midbody, expression is observed in motor neurons of the VNC, and other neurons, as labeled. *e*, In the tail of the adult, TagRFP is also observed in the ventral neurons, phasmid socket, and rectal gland. *f*, Expression of TagRFP (magenta) is observed in GABAergic motor neurons labeled with punc-25::GFP (green). *g*, Expression of TagRFP (magenta) is observed in cholinergic motor neurons labeled with punc-17::GFP (green). *h*, Expressed panneuronally under the prab-3 promoter, GFP fused to the N- or C-terminal ends of *phac-1* (top) is observed in the cytoplasm and neurites of neurons and excluded from the nucleus. A constitutively active *gsp-1::phac-1::GFP* fusion construct (bottom) shows similar distribution, suggesting the constitutive PP1-PHAC-1 holoenzyme remains cytoplasmic.

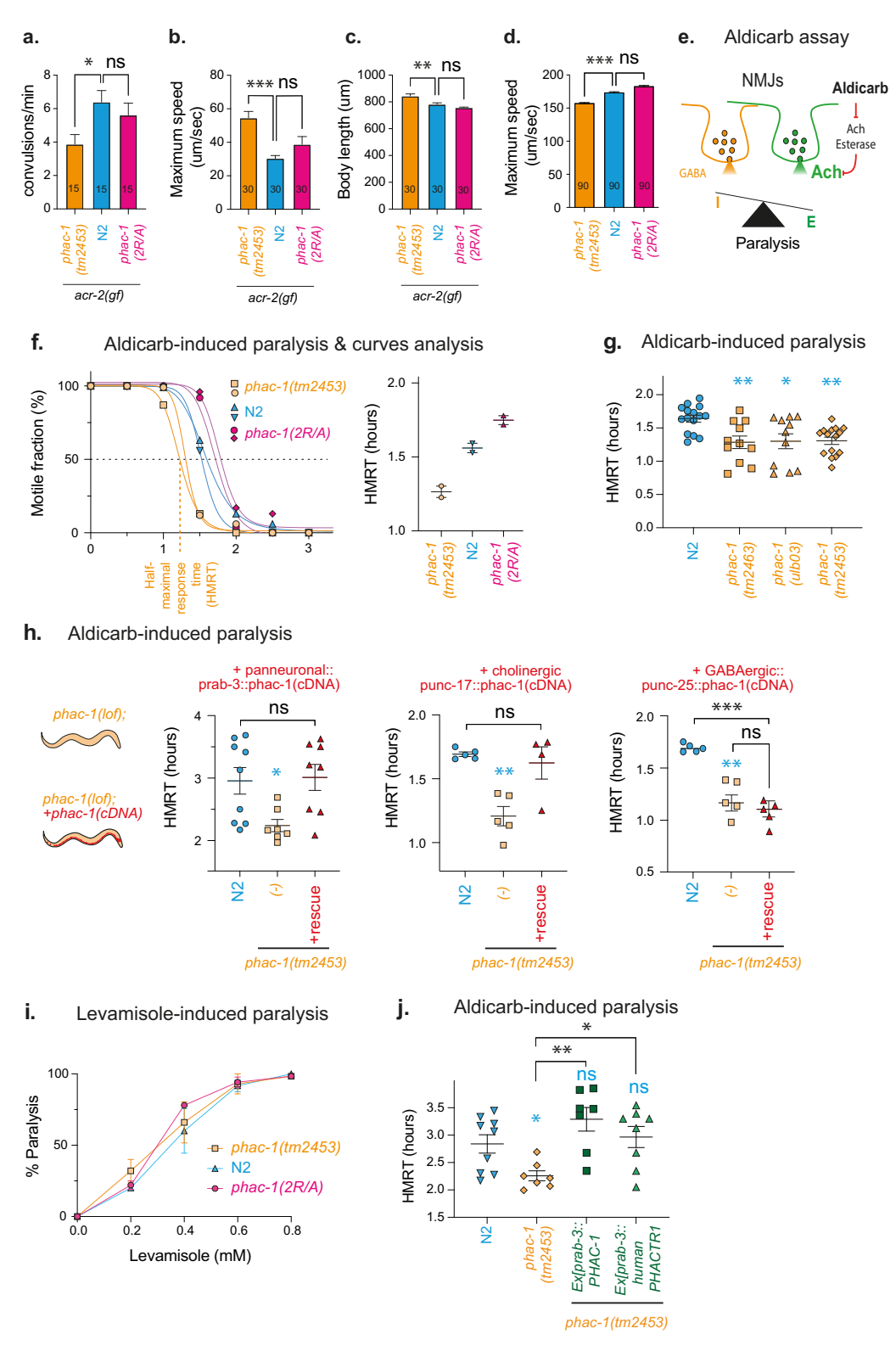


Figure 4. PHAC-1 regulates locomotion speed and the E/l balance in the motor circuit of *C. elegans.* \boldsymbol{a} , Quantification of convulsion frequency in genotypes as indicated. The convulsion rate is reduced in acr-2(gf); phac-1(tm2453) compared with acr-2(gf); \boldsymbol{b} , The speed of forward locomotion is improved in acr-2(gf); phac-1(tm2453) compared with acr-2(gf); \boldsymbol{c} , The hypercontraction of the body of acr-2(gf) is reduced in acr-2(gf); phac-1(tm2453). \boldsymbol{d} , The forward locomotion speed of phac-1 mutants exposed to 1% 0_2 : phac-1(lf) animals displays reduced locomotion speed compared with N2 controls. N=90 individuals. Data in $4\boldsymbol{a}-\boldsymbol{d}$ are plotted as the means \pm SEM for the indicated number (N) of animals. Statistics use one-way ANOVA and Tukey's for multiple-comparison tests. $*: p \le 0.05$, $**: p \le 0.05$, $**: p \le 0.01$, $**: p \le 0.001$. \boldsymbol{e} , The aldicarb assay was used to detect differences in neurotransmission at the NMJ. Aldicarb inhibits acetylcholinesterase, leading to the accumulation of ACh in the synaptic cleft, which produces paralysis. The rate of paralysis reflects the strength of ACh and GABA signaling at the NMJ. \boldsymbol{f} , The rate of paralysis is determined for groups of 20-25 animals. For each independent group, we determined the time for HMRT to aldicarb from nonlinear regression curves (sigmoidal, 4PL). The HMRT values are then displayed in scatterplots. \boldsymbol{g} , All phac-1 deletion-mutant strains are hypersensitive to 0.5 mM aldicarb compared with N2 controls. Comparisons with N2 are displayed in blue. \boldsymbol{h} , The hypersensitivity of phac-1 null mutants to 0.5 mM aldicarb is rescued by the expression of phac-1 cDNA in GABAerqic neurons using the unc-25 promoter (right). Comparison with N2 is displayed in blue.

or hypersensitivity to aldicarb paralysis can reflect changes in ACh, GABA, and/or neuropeptide signaling at the NMJ (Mahoney et al., 2006; Fig. 4e). We analyzed the time for paralysis in the presence of aldicarb. For all replicates, we determined the time at which 50% of animals (N=20) are paralyzed (Fig. 4f). All phac-1 deletion mutants tested caused similar aldicarb-hypersensitive phenotypes, suggesting PHAC-1 regulates NMJ signaling (Fig. phac-1(tm2463), p = 0.0099; phac-1(ulb03), p = 0.0147; phac-1(tm2453), p = 0.0083). Despite the broad expression of phac-1, the aldicarb response in phac-1(tm2453) mutants was completely restored by panneuronal or cholinergic expression of phac-1 cDNA (Fig. 4h; panneuronal rescue vs N2, p = 0.8369; cholinergic rescue vs N2, p = 0.82; other p-values in Extended Data 2). Selective expression of phac-1 cDNA in GABAergic neurons did not alter significantly the aldicarb responses (Fig. 4h; GABAergic rescue vs N2, p = 0.0002; GABAergic rescue vs phac-1(lf), p =0.428). The muscle sensitivity to the ionotropic cholinergic agonist levamisole was not significantly altered in phac-1 mutants (Fig. 4i; phac-1(lf), p = 0.9909; phac-1(2R/A), p = 0.9874). Taken together, these results suggest that aldicarb hypersensitivity in phac-1(tm2453) mutants corresponds to abnormal cholinergic NMJ signaling rather than a defect in muscle response. To evaluate the conservation of PHACTR function, we attempted to rescue phac-1(tm2453) with the human gene. Panneuronal expression of human PHACTR1 cDNA rescued the aldicarb hypersensitivity of phac-1(tm2453), suggesting that at least some PHACTR functions are conserved in neurons (Fig. 4j; panneuronal human cDNA rescue vs N2, q = 0.4186; panneuronal human cDNA rescue vs phac-1(lf), q = 0.0189).

Mutations in *phac-1* that mimic the human DEE70 variants generate a constitutively active holophosphatase

PHACTRs cycle between an active PP1-PHACTR holophosphatase and an inactive G-actin-PHACTR complex, depending on the local concentration of G-actin bound to RPEL motifs (Mouilleron et al., 2012; Wiezlak et al., 2012; Huet et al., 2013; Fig. 5a). Human genetic studies previously revealed four heterozygous dominant de novo mutations in PHACTR1 associated with DEE70 syndrome. These four mutations correspond to substitutions of highly conserved amino acids located within the last two RPEL motifs (Hamada et al., 2018; Marakhonov et al., 2021). Mutation of the arginine (R) of the RPEL motifs prevents G-actin binding to human PHACTR1/4 and induces the constitutive binding of PP1 (Wiezlak et al., 2012; Huet et al., 2013). We engineered a phac-1(2R/A) allele (R469A combined with R507A) where the R of the last two RPEL motifs of phac-1 were replaced by alanines (A) as done in Mouilleron et al. (2012) and Huet et al. (2013). We compared the effects of 2R/A mutations to deletion alleles (Fig. 5b). The phac-1(2R/A) allele caused aldicarb resistance, contrasting with phac-1 deletion mutants that were all aldicarb hypersensitive (Fig. 5b; phac-1(2R/A) vs N2, q = 0.0049; phac-1(tm2453) vs N2, q < 0.0001). In several behavioral readout, the *phac-1*(2R/A) allele behaved unlike the *phac-1*(tm2453) deletion mutant: the phac-1(2R/A) allele did not rescue the flp-18(XS) (Fig. 1f) nor the acr-2(gf) phenotypes (Fig. 4a, p = 0.1607; Fig. 4b, p = 0.2673; Fig. 4c, p = 0.1077). While phac-1(tm2453) reduces the maximal speed of locomotion, phac-1(2R/A) tends to increase it (Fig. 4d; p = 0.555). We then replicated three amino acid substitutions of the human DEE70 variants in the C. elegans phac-1 gene using CRISPR-Cas9. These three phac-1 alleles mimicking L500P, L519R, and R521C variants caused aldicarb resistance, like phac-1(2R/A) (Fig. 5b, R521C vs N2: q = 0.0092; Fig. 5c, L500P vs N2: q = 0.0014, L519R vs N2: q = 0.0032). Conversely, a phac-1 R536P mutation, which mimics a hypomorphic allele of PHACTR4 that prevents PP1 binding (Kim et al., 2007), caused a weak but significant aldicarb hypersensitivity similar to the deletion alleles (Fig. 5b, q = 0.0219). Therefore, R536P caused a loss of function phenotype, likely by diminishing the formation of the PP1-PHAC-1 holophosphatase. Conversely, DEE70 mutations and 2R/A mutations induced a gain-of-function (gf) phenotype, likely by promoting the constitutive formation of the PP1-PHAC-1 holophosphatase. Overexpression of phac-1(2R/A) cDNA in all neurons, or in cholinergic motor neurons, caused aldicarb resistance in the N2 background, suggesting a dominant-positive mode of action (Fig. 5*d*; panneuronal expression, q = 0.0037; cholinergic expression, q = 0.0059). Additionally, heterozygous animals for phac-1(L500P/+) and phac-1(2R/A/+) were also aldicarb resistant compared with N2 controls (Fig. 5e; L500P/+, q = 0.0258; phac-1(2R/A/+), q = 0.0125).

Given the competition between G-actin and PP1 for binding to PHACTRs, mutated RPEL motifs are expected to reduce G-actin binding and to promote PP1 binding (Fig. 5a). To gain support for the interpretation that DEE70 and 2R/A mutations cause aldicarb resistance by promoting the constitutive binding of PP1 to PHAC-1, we generated a protein fusion in which PHAC-1 is constitutively fused to GSP-1, one of the four PP1 catalytic subunits of C. elegans. Panneuronal expression of this fusion protein in phac-1(tm2453) induced aldicarb resistance, as observed in phac-1(DEE70) alleles and in phac-1(2R/A) (Fig. 5f, q = 0.0002). A D64A mutation within the PP1 catalytic site reduces its enzymatic activity (Zhang et al., 1996). The panneuronal expression of a mutated PHAC-1-PP-1(D64A) construct in phac-1(tm2453) had no effect (Fig. 5f; phac-1(tm2453) vs Ex[prab-3::PP1-PHAC-1(D64A)], q = 0.142), suggesting PP1 enzymatic activity is required for the fusion protein to confer aldicarb resistance. As the DEE70 and 2R/A alleles mimic the aldicarb resistance observed by PP1-PHAC-1 fusion, we conclude that the DEE70 and 2R/A alleles generate PHAC-1 variants that bind PP1 constitutively. We next asked how the gain of function allele phac-1(2R/A) disturbed NMJ signaling. It could act in neurodevelopment and in neuronal or synaptic function. To determine the temporal requirements of PHAC-1 signaling, we induced phac-1(2R/A) expression at larval stage 1 (L1) or in adulthood (Fig. 5g). The induction of phac-1(2R/A) in N2 adults led to aldicarb resistance as in phac-1(2R/A) (Fig. 5g, not induced vs L4 induced, q = 0.0002), while induction in the early larval stage did not (Fig. 5g, not induced vs L1 induced, q = 0.1885). A weak expression of the transgene was observed in noninduced animals, which explains the aldicarb resistance observed in the

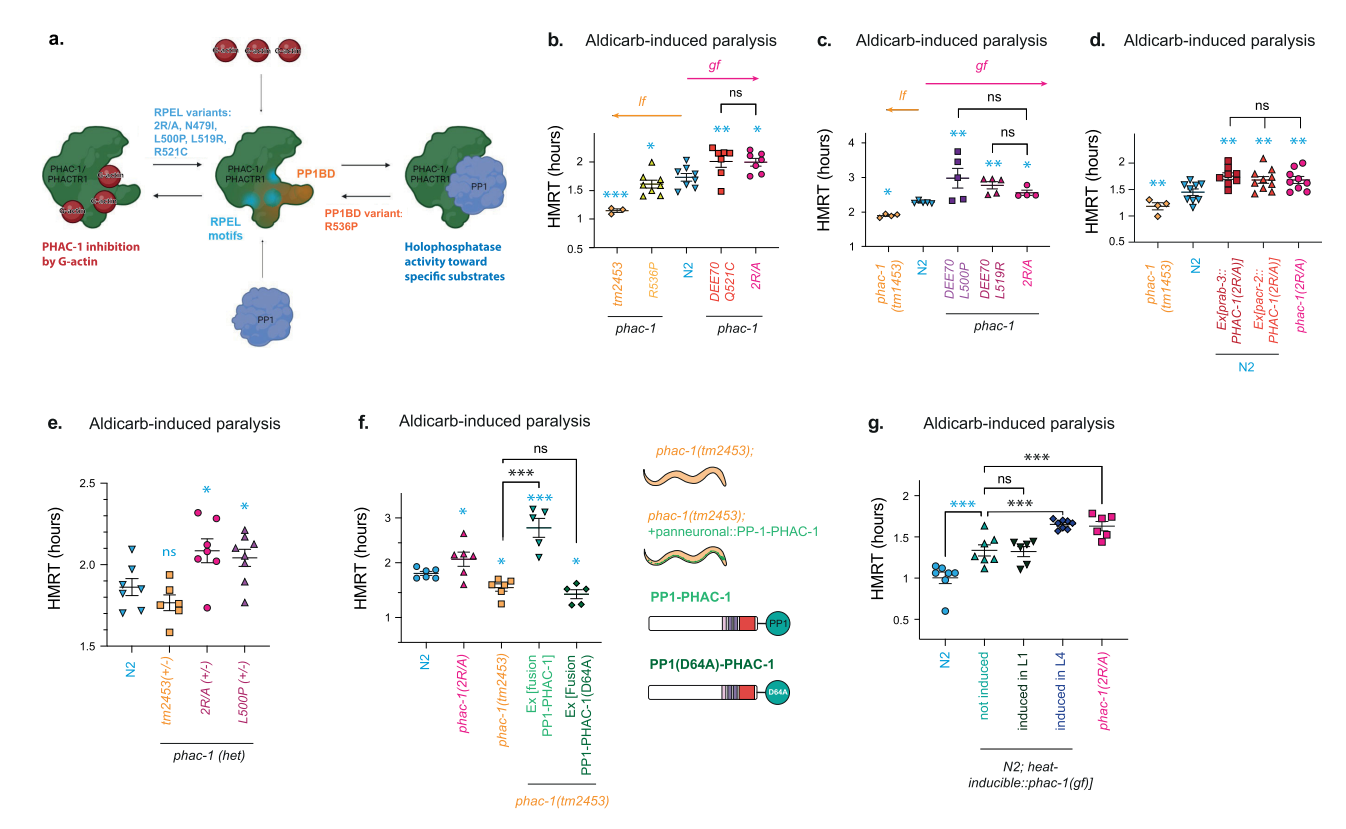


Figure 5. Mutations in *phac-1* that mimic the human DEE70 variants generate a constitutively active holophosphatase. a, Model of PHACTR-PP1 holoenzyme regulation. According to this model, mutations alter the balance between G-actin and PP1 binding to PHACTRs. Mutations within the PP1 binding domain (humdy) prevent PP1 binding and therefore reduce holophosphatase activity; mutations within the RPEL motifs prevent G-actin binding and therefore favor PP1 binding and the holophosphatase activity (including DEE70 variants *N4791*, *L500P*, *L519R*, and *R521C*). b, c, As phac-1(tm2453) deletion mutant, the humdy/*R536P* mutation causes sensitivity to aldicarb suggesting loss of function alleles. In contrast to the phac-1(tm2453) deletion mutant, the G-actin-binding-deficient mutant phac-1(2R/A) causes resistance to aldicarb, suggesting a gf allele. Comparisons with N2 are displayed in blue. See Figure 2a, b for a model explaining the phac-1 mutations tested in the following experiments. b, The Q521C mutation mimicking the R521C DEE70 also causes aldicarb resistance, while the humdy/*R536P* mutation causes a weak hypersensitivity to 1 mM aldicarb. c, The L500P and L519R mutations mimicking the DEE70 L500P and L519R, respectively, cause resistance to 0.5 mM aldicarb. c, Panneuronal or cholinergic expression of a phac-1(2R/A) cDNA in the N2 background causes resistance to 1 mM aldicarb, suggesting a dominant-positive mode of action for the 2R/A mutation. Comparisons with N2 are displayed in blue. c, Panneuronal expression of PP1-PHAC-1 fusion proteins, where PP1 corresponds to c-1. Panneuronal expression of a PP1-PHAC-1 fusion protein in c-1 fusion proteins, where PP1 corresponds to c-1. Panneuronal expression of a PP1-PHAC-1 fusion protein in c-1 fusion protein construct carrying a D64A mutation that reduces c-1 expression in the absence of heac-1 c-1 expression in the absence of heac-1 expression of c-1 expression in the absence of heat induction. Scatterplots

absence of induction. These results suggest phac-1(2R/A) acts postdevelopmentally in the adult to regulate NMJ function. For simplicity, in the following sections, we refer to phac-1(tm2453) as phac-1(lf) and phac-1(2R/A) as phac-1(gf).

phac-1 signaling alters the ultrastructure and the function of NMIs

Aldicarb exposure revealed altered NMJ transmission, suggesting an E/I imbalance in the *phac-1* mutants. To better define the effects of *phac-1* signaling at the NMJ, we used a combination of quantitative fluorescence imaging, electron microscopy, and electrophysiology. We first determined the effects of *phac-1* on the cell biology of the DA cholinergic motor neurons using a panel of strains expressing integrated presynaptic markers (Sieburth et al., 2005; Ch'ng et al., 2008). The dorsal axons of the DA motor neurons form stereotypical en passant NMJs (Fig. 6a). Peaks of fluorescence intensity along these dorsal axons, representing synaptic puncta, were analyzed for each fluorescently tagged marker protein. We did not observe significant differences in the peak fluorescence intensity of the active

zone marker UNC-10-GFP (ortholog of vertebrate RIM; Fig. 6b; phac-1(lf), p = 0.5924; phac-1(gf), p = 0.326) nor in the peak density of UNC-10-GFP puncta (Fig. 6c; phac-1(lf), p = 0.32; phac-1(gf), p = 0.9778). This suggests that neither the density nor the size of active zones is altered in *phac-1* mutants. To quantify presynaptic SV pools, we used the SV-associated RAB-3-GFP marker. RAB-3-GFP peak fluorescence showed a significant decrease in phac-1(gf), suggesting reduced SV pools in phac-1(gf) (Fig. 6d; p = 0.0048). The density of RAB-3-GFP peak was not modified (Fig. 6e; phac-1(lf), p = 0.8515; phac-1(gf), p = 0.3955), suggesting the density of presynaptic boutons is altered in phac-1 mutants. To support a potential imbalance of SV exocytosis and endocytosis in phac-1(gf) mutants in vivo, we used the pH-sensitive synaptobrevin/SNB-1-pHluorin marker expressed in cholinergic motor neurons. The integral membrane protein SNB-1-pHluorin cycles between the SV membrane and the plasma membrane during the SV cycle. As SNB-1-pHluorin fluorescence is quenched within the acidic environment of the SV lumen, the fluorescent signal reflects pHluorin in the plasma membrane exposed to the extracellular milieu at a

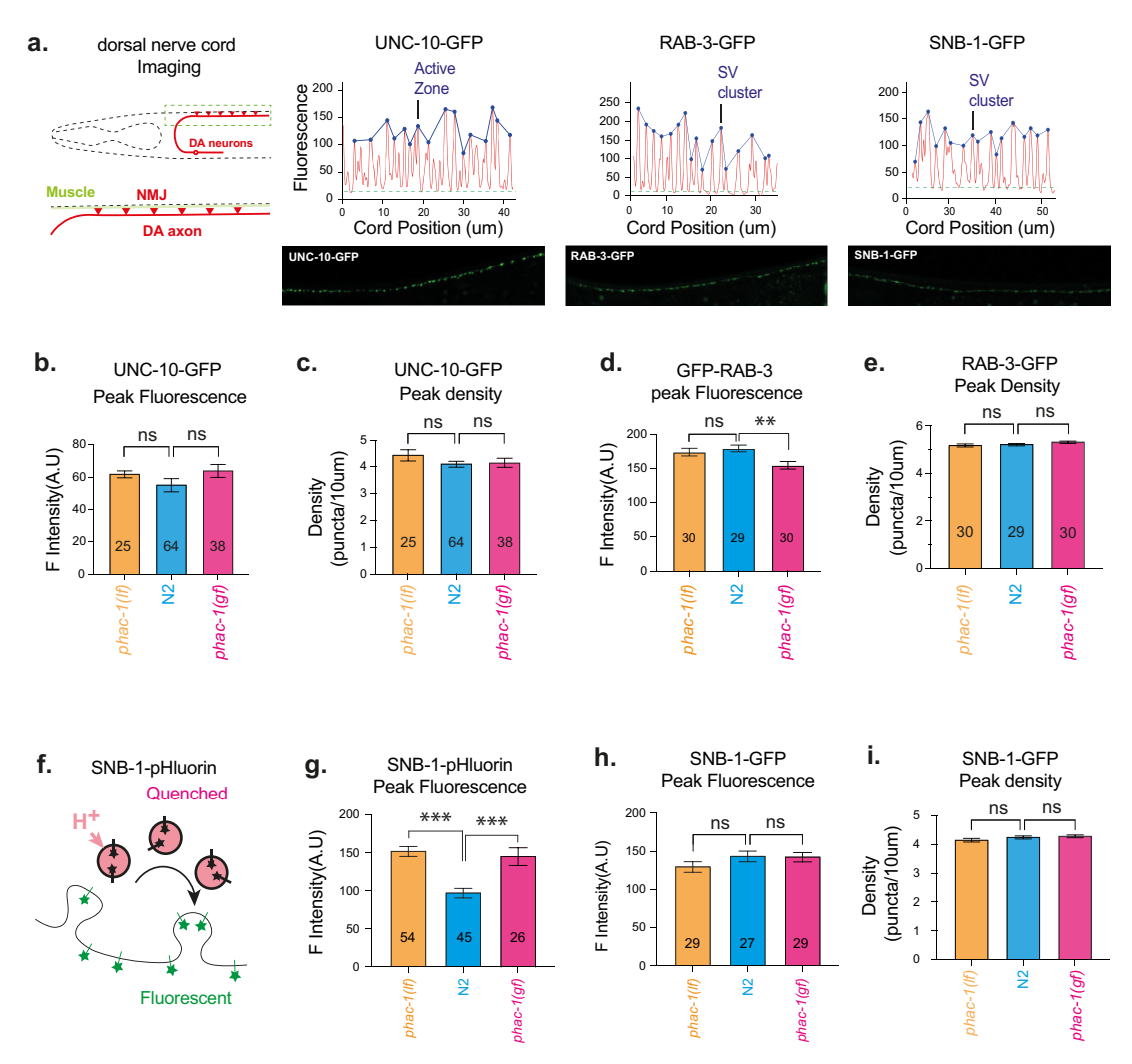


Figure 6. *phac-1* signaling alters SV pool without affecting synaptogenesis. *a*, Schematic representation of the dorsal NMJs formed by the DA cholinergic motor neurons along the dorsal nerve cord (DNC), where imaging of synaptic markers was performed. Representative images show the fluorescence of the active zone marker UNC-10-GFP and the SV markers RAB-3-GFP and SNB-1-GFP along the DNC. The fluorescence intensity and density along the DNC display peaks corresponding to local enrichment of these presynaptic markers and the density of presynaptic terminals (see Materials and Methods for peak detection). Additional parameters not plotted here are available in Extended Data 2 for UNC-10-GFP, RAB-3-GFP, SNB-1-pHluorin, and SNB-1-GFP. b, The fluorescence intensity of UNC-10-GFP peaks is not modified in *phac-1* mutants compared with N2. c, The peak density of UNC-10-GFP along the DNC is not modified in *phac-1* mutants compared with N2. d, The fluorescence intensity at RAB-3-GFP peaks is significantly reduced in *phac-1(gf)* compared with N2, indicating a reduced SV pool. e, The peak density of RAB-3-GFP along the DNC is not modified in *phac-1* mutants compared with N2. f, To probe the SV cycle, we used the pH-sensitive marker SNB-1-pHluorin, which is quenched in the acidic environment of the SVs. Its fluorescence reports the fraction of SNB-1 at the plasma membrane and reflects the balance between SV exocytosis and endocytosis. g, The peak fluorescence intensity of SNB-1-GFP is not altered in the DNC of *phac-1* mutants compared with N2. i, The peak density of SNB-1-GFP along the DNC is not altered in the DNC of *phac-1* mutants. For all presynaptic markers quantified in data 6c, e, j, we observe a similar density (4–5 presynaptic terminals/10 μm) in N2 and *phac-1* mutants. Data are plotted as the mean ± SEM; the number of individuals analyzed is indicated. One-way ANOVA and Tukey's for multiple comparisons. ns, p > 0.05; **, $p \le 0.05$; **, $p \le 0.05$; **, $p \le 0.00$; ***, $p \le 0.00$ 1.

neutral pH. Thus, SNB-1-pHluorin fluorescence can reflect the balance between SV exocytosis and endocytic rates (Fig. 6f; Kavalali and Jorgensen, 2014). We observed increased SNB-1-pHluorin peak fluorescence in dorsal cholinergic NMJs of both phac-1(lf) (p < 0.0001) and phac-1(gf) (p = 0.0003) mutants (Fig. 6g). Unlike SNB-1-pHluorin fluorescence, the intensity of SNB-1-GFP peak fluorescence showed no significant differences between phac-1 mutants and control animals (Fig. 6h; phac-1(lf), p = 0.3211; phac-1(gf), p = 0.9955). The density of SNB-1-GFP peak was not modified (Fig. 6i; phac-1(lf), p = 0.3897; phac-1(gf), p = 0.8779). Supporting normal synaptogenesis, none of the presynaptic markers showed altered density (Fig. 6c,e,i).

We used transmission electron microscopy (TEM) after highpressure freeze fixation to define the ultrastructure of the NMJs (Fig. 7a). Our analysis confirmed that the overall ultrastructural integrity of the ventral cholinergic NMJs was preserved in *phac-1* mutants, but subtle differences in morphological parameters were apparent. We observed larger presynaptic terminals in *phac-1(lf)* compared with N2 (Fig. 7b; p < 0.0001), but a similar dense projection (DP) area (Fig. 7c; *phac-1(lf)*, p = 0.3183; *phac-1(gf)*, p = 0.3001). We observed a marked reduction in the total number of SVs in *phac-1(gf)* compared with N2 (Fig. 7d; p = 0.0001). We also observed an increase in the average SV diameter in *phac-1(lf)* (p < 0.0001) and *phac-1(gf)* (p < 0.0001) compared with N2 (Fig. 7e). Together, these observations are suggestive of alterations in SV recycling and/or sorting processes, which may explain the SNB-1-pHluorin recapture defect and the reduced SV pool in *phac-1(gf)* (Yu et al., 2018; Li et al., 2021; Zhang et al., 2022). However, we did not observe changes for the number of synaptic endosomes (Fig. 7f; *phac-1(lf)*, p = 0.9989;

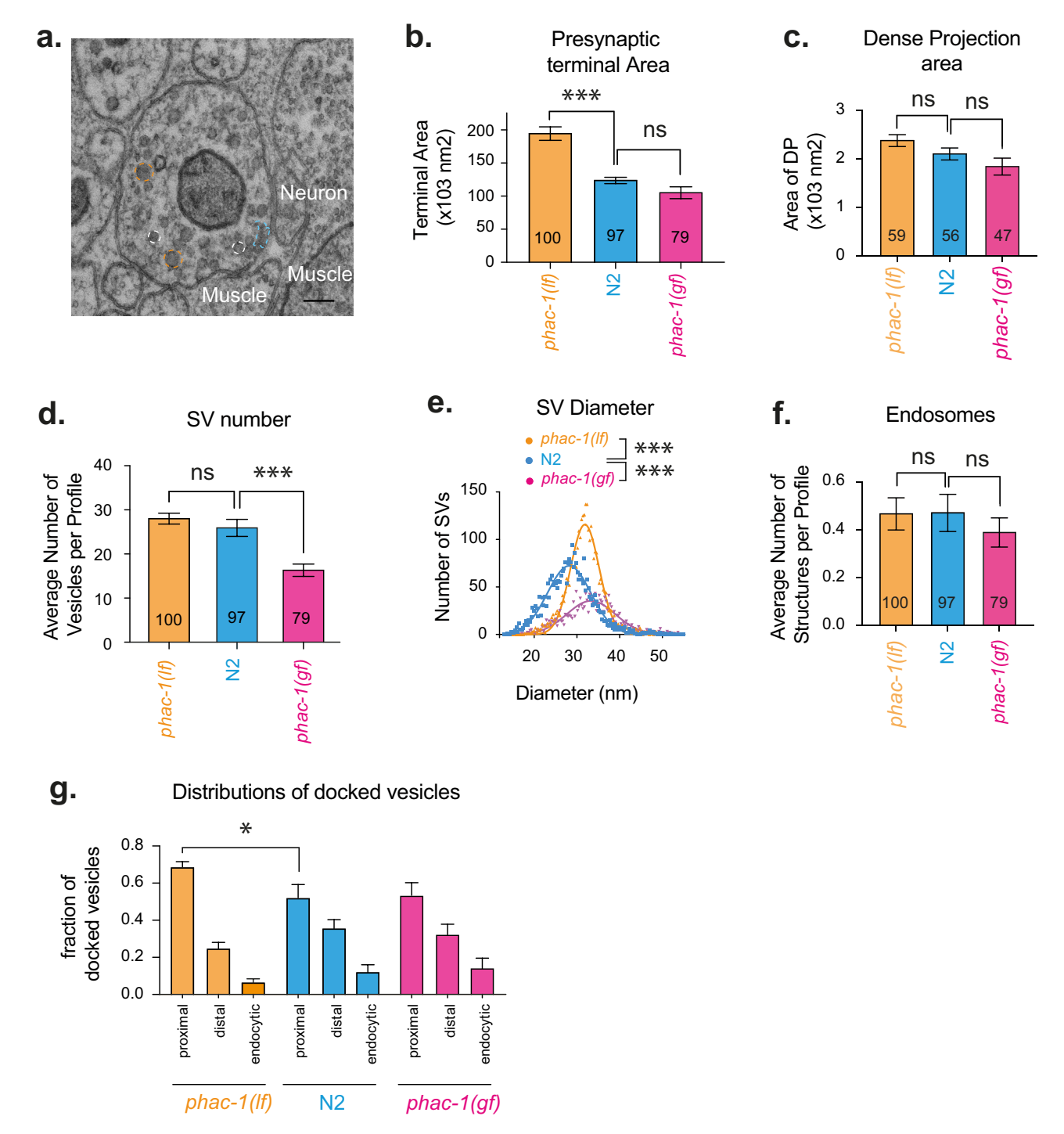


Figure 7. Electron microscopy imaging reveals defects in synapse ultrastructure and SV pool maintenance in phac-1 mutants. a, The ultrastructure of cholinergic synapses at the ventral neuromuscular junction was observed by electron microscopy. In this representative cross section, we highlight SV (white), DCVs (orange), and DP (blue). These ROIs were used for 3D reconstructions. b, It revealed an increased presynaptic terminal area in phac-1(lf) compared with N2. c, The DP area is not altered in phac-1 mutants compared with N2. d, The average number of SV per TEM profile containing a DP shows a strong reduction in phac-1(lf) mutants. e, The diameter of individual SV is plotted; the mean diameter of the SVs was larger in phac-1(lf) and (gf) mutants compared with N2 (Gaussian nonlinear fit: 31.8, 33.3, and 28.2 nm diameter, respectively) suggestive of SV recycling defects. f, The number of endosomes is not modified in phac-1 mutants compared with N2 controls. g, The fraction of docked SVs in the proximal (0–90 nm), the distal (91–300 nm), and the endocytic (301–500 nm) zones relative to the DP indicates a higher proportion of SVs primed next to the DP in phac-1(lf). Data on b, c, d, f, g represent the mean and SEM. One-way ANOVA and Tukey's (7b-f) or Games—Howell's (7g) for multiple comparisons. ns, p > 0.05; **, $p \le 0.05$; **, $p \le 0.05$; **, $p \le 0.01$; ***, $p \le 0.01$; ***, $p \le 0.01$;

phac-1(gf), p = 0.7025). A slight increase was observed for the proportion of vesicles docked proximal to the active zone in *phac-1(lf)* (Fig. 7*g*; p = 0.0172). To ascertain whether and how these ultrastructural alterations affect ACh and GABA release, we conducted patch-clamp recordings of the body-wall muscle

cells. We monitored spontaneous miniature postsynaptic currents (mPSCs) as well as stimulus-evoked excitatory postsynaptic currents (EPSCs; Richmond et al., 1999; Martin et al., 2011; Fig. 8a). phac-1 signaling did not modify the frequency (Fig. 8b; phac-1(lf), p=0.5978; phac-1(gf), p=0.9708) and

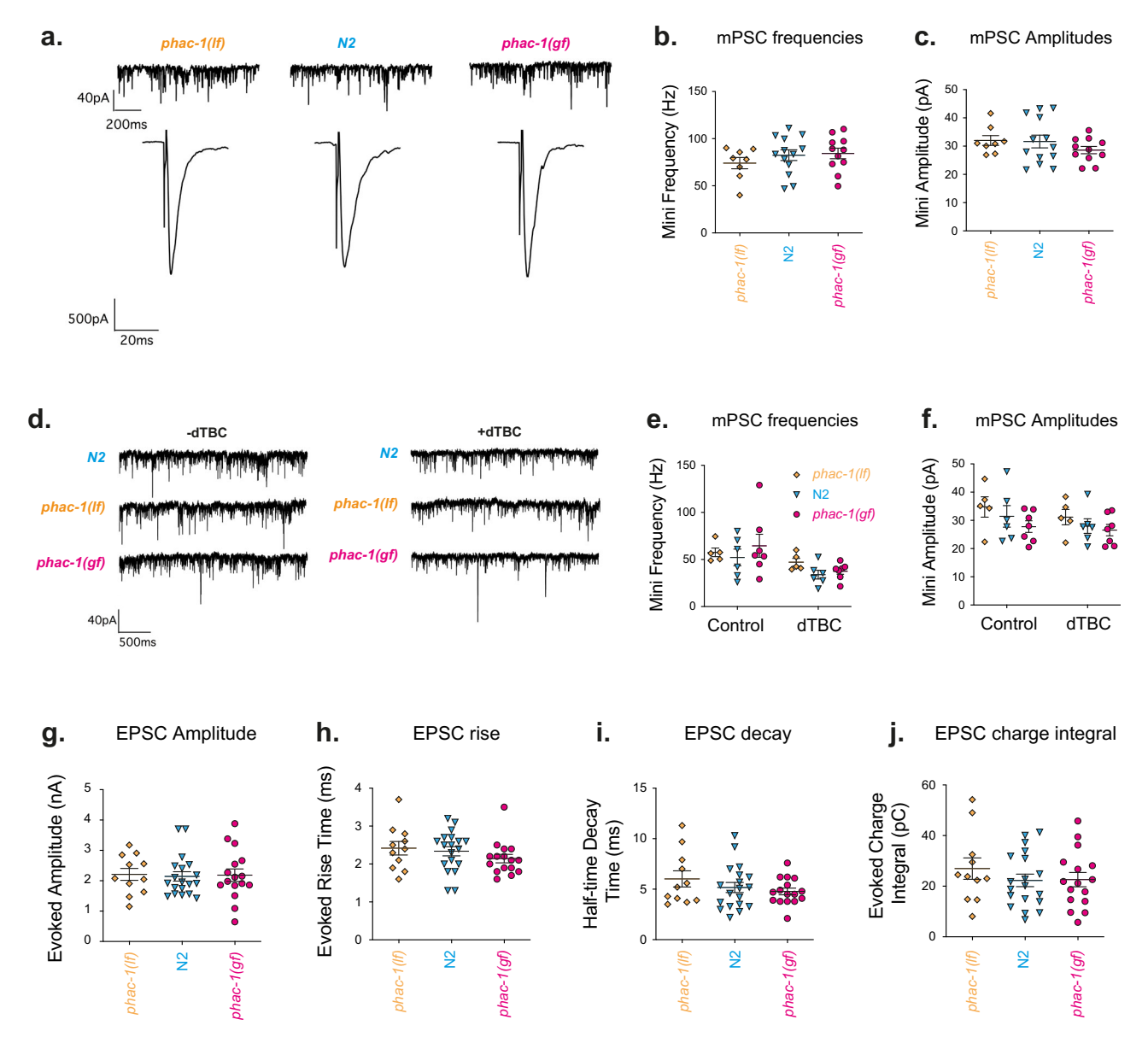


Figure 8. SV exocytic properties are not modified ex vivo in phac-1 mutants. a, Spontaneous mPSCs (above) and EPSCs (below) were recorded by patch clamping the body wall muscle in N2 and phac-1(lf) and phac-1(gf) mutants. b, c, The mPSC frequency (b) and amplitude (c) were not modified in phac-1 mutants compared with N2. d, To distinguish between cholinergic and GABAergic minis, mPSCs were recorded before and after perfusion of the cholinergic receptor antagonist dTBC. In the presence and in the absence of dTBC, the mPSC frequency (c) and amplitude (c) were not modified in c0 mutants compared with N2. c0 mutants compared with N2. c0 mutants compared with N2. Scatterplots correspond to the vNC. The quantification does not reveal differences in EPSC amplitude (c0), rise time (c0), half-time decay (c0), and charge transfer (c0), in c0 mutants compared with N2. Scatterplots correspond to the values measured in each animal. Bar and whiskers represent mean c1 mutants and Tukey's (c1) or Dunn's (c2) mutants compared with N2. Scatterplots correspond to the values measured in each animal. Bar and whiskers represent mean c3 mutants compared with N2. Scatterplots correspond to the values measured in each animal. Bar and whiskers represent mean c3 mutants compared with N2. Scatterplots correspond to the values measured in each animal. Bar and whiskers represent mean c4 mutants compared with N2. Scatterplots correspond to the values measured in each animal. Bar and whiskers represent mean c5 mutants compared with N2. Scatterplots correspond to the values measured in each animal. Bar and whiskers represent mean c5 mutants compared with N2. Scatterplots correspond to the values measured in each animal. Bar and whiskers represent mean c6 mutants compared with N2. Scatterplots correspond to the values measured in each animal mutants compared with N2.

amplitude of mPSCs (Fig. 8c; phac-1(lf), p = 0.9914; phac-1(gf), p = 0.4746). To reveal GABA currents, we analyzed the mPSCs before and after treatment with dTBC, which blocks ACh receptors (Fig. 8d). The mPSC frequency and amplitude were not altered by phac-1 signaling before or after dTBC treatment (frequency after dTBC: Fig. 8e, phac-1(lf): p = 0.4838, phac-1(gf): p = 0.9353; amplitude after dTBC: Fig. 8f, phac-1(lf): p = 0.7213, phac-1(gf): p = 0.9253). Finally, phac-1 signaling did not modify the amplitude, kinetics, or charge integral of EPSCs (amplitude: Fig. 8g, phac-1(lf): p > 0.9999, phac-1(gf): p > 0.9999; rise time: Fig. 8h, phac-1(lf): p > 0.9999, phac-1(gf): p = 0.3100; decay time: Fig. 8i, phac-1(lf): p = 0.5267, phac-1(gf): p = 0.8349; charge integral: Fig. 8j, phac-1(lf): p = 0.5539, phac-1(gf): p = 0.9966). Therefore, phac-1 mutants do not affect the SV exocytic properties from cholinergic and GABAergic NMJs under these

recording conditions. One potential explanation for the discrepancy between the electrophysiology and the imaging results is the diffusion of neuromodulators resulting from the dissection, which exposes the NMJs to extracellular solution.

phac-1 affects neuropeptide secretion and DCV dynamics

To probe the effects of PHAC-1 signaling on neuropeptide release, we combined quantitative fluorescence imaging and electron microscopy. To observe the DCV pool in vivo, we used strains expressing the NLP-21-Venus neuropeptides transported and released by DCVs. We did not observe changes in the soma fluorescence (phac-1(lf), p=0.5853; phac-1(gf), p=0.7868; Fig. 9a). Along the DA axons of phac-1(gf), the total fluorescence intensity was reduced for NLP-21-Venus (p=0.0016), suggesting increased neuropeptide release (Fig. 9b). Compared with the

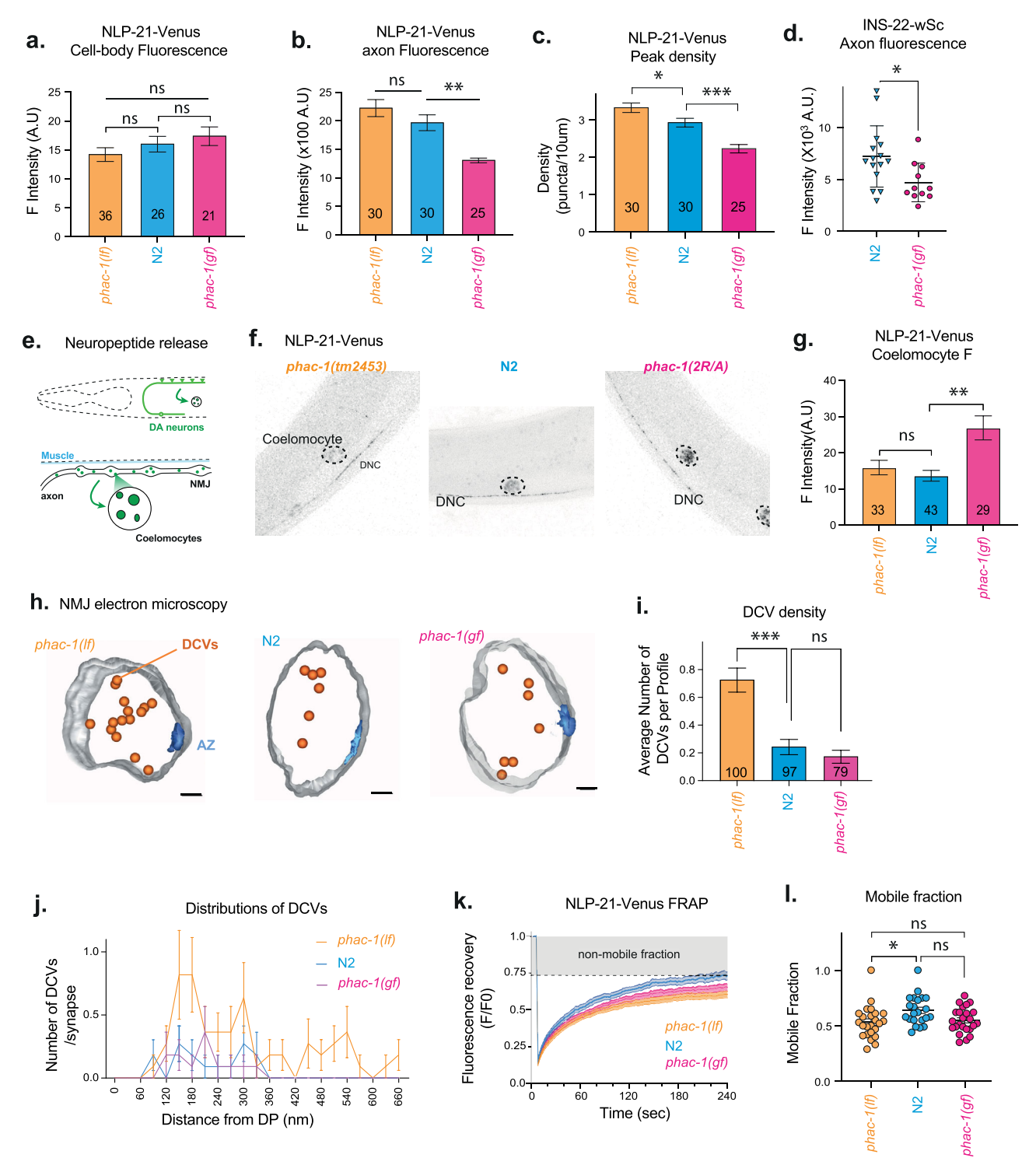


Figure 9. PHAC-1 signaling alters the axonal distribution of DCV and promotes neuropeptide release. a, The fluorescence intensity of the neuropeptide/DCV marker NLP-21-Venus in the cell body is not altered in phac-1 compared with N2. b, The total axonal fluorescence intensity of NLP-21-Venus is significantly reduced along the DA axon of phac-1(gf) compared with N2. c, The NLP-21-Venus fluorescence peaks—corresponding to DCVs—are more distributed along the DA axon in phac-1(ff) than in controls and phac-1(gf). More parameters on NLP-21-Venus are available in Extended Data 2. d, As for NLP-21-Venus, the total fluorescence intensity of the neuropeptide/DCV marker INS-22-wSc is significantly reduced along the DA axon of phac-1(gf) compared with N2. e, Coelomocytes cells scavenge tagged neuropeptides released in the pseudocoelomic cavity; NLP-21-Venus fluorescence in coelomocytes is a proxy for NLP-21-Venus release. f, Representative images showing fluorescence of the DCV marker NLP-21-Venus along the DNC and in the coelomocytes of N2 and phac-1 mutants. g, The fluorescence intensity of NLP-21-Venus in coelomocytes is increased in phac-1(gf) compared with N2, suggesting increased neuropeptide release. f, Representative 3D reconstructions of the cholinergic synapses showing increased number of DCVs (orange) away from DP (blue) in phac-1(ff) compared with N2. All scale bars are 100 nm. f, The average number of DCVs per TEM profile is increased in phac-1(ff) compared with N2. f, The distribution of DCVs along the axon relative to DP suggests DCVs accumulate away from the presynaptic terminals in phac-1(ff). f, The fluorescence recovery after the photobleaching of NLP-21-Venus over a portion of the DA axon corresponds to the exchangeable/mobile fraction of DCVs. f, The mobile fraction is significantly reduced in phac-1(ff) compared with N2. Data are plotted as the mean \pm SEM; the number of individuals or EM profile analyzed is indicated. Scatterplot on g corresponds to

density of the other presynaptic markers (4–5 per 10 μm) the low density of NLP-21-Venus peaks in phac-1(gf) suggests several presynaptic terminals lack neuropeptide-loaded DCVs (Fig. 9c; N2 vs phac-1(gf), p=0.0003)). Conversely, DCV density was higher in phac-1(lf) than in N2 (p = 0.0469). We confirmed the effects of phac1 signaling on neuropeptides with the neuropeptide marker INS-22-wSc. As for NLP-21-Venus, the INS-22-wSc fluorescence was reduced along the DA axon in phac-1(gf) (Fig. 9d; p = 0.0488). As a proxy to quantify NLP-21-Venus neuropeptide release, we measured the Venus fluorescence intensity in coelomocytes, known to scavenge NLP-21-Venus released by DA neurons into the pseudocoelomic cavity (Fig. 9e,f; Sieburth et al., 2005; Laurent et al., 2018). We observed an increased NLP-21-Venus fluorescence intensity in coelomocytes of phac-1(gf) (Fig. 9g; p = 0.002). Altogether, reduced axonal NLP-21-Venus fluorescence and increased NLP-21-Venus scavenging by coelomocytes in phac-1(gf) suggest phac-1(gf) releases more neuropeptides than controls. The ultrastructure analysis of cholinergic NMJs supports the NLP-21-Venus data: compared with N2, we observed an increased number of DCVs in the synaptic profiles of phac-1(lf) mutants (Fig. 9h,i; phac-1(lf) vs N2, p < 0.0001). In *phac-1(lf)* mutants, these additional DCVs were observed to spread further along the axon from the DPs (Fig. 9j).

The number and the distribution of DCVs depend on their traffic, capture, and exocytosis along the axon (Wong et al., 2012; Bulgari et al., 2014). To probe the effects of PHAC-1 signaling on DCV mobility, capture, and exocytosis, we performed a FRAP assay over 12 μ m of the DA axon, including \sim 6 presynaptic terminals. Upon photobleaching, we observed gradual recovery of NLP-21-Venus fluorescence, indicating the mobilization and capture of transiting NLP-21-GFP-loaded DCVs. However, the extent of fluorescence recovery remains limited, suggesting \sim 30% of the bleached DCVs were stationary—or captured—in N2 (Fig. 9k,l). The mobile fraction of DCVs extracted from FRAP curves was reduced in *phac-1(lf)* (Fig. 9l; p = 0.0204), suggesting *phac-1* signaling regulates DCV capture in axon and presynaptic terminals.

Although the molecular identity of the "tethering elements" capturing DCVs is unclear, synapsin/SNN-1 and F-actin are implicated (Bittins et al., 2010; Anbalagan et al., 2019; Yu et al., 2021). PHACTRs control the F-actin dynamics via the dephosphorylation of the severing enzyme cofilin (Huet et al., 2013). To explain the differential release of neuropeptide in phac-1(lf) and phac-1(gf), we hypothesized differential remodeling of F-actin and/or synapsin in phac-1(lf) and phac-1(gf) mutants. To observe a remodeling of synapsin and F-actin, we designed a strain coexpressing SNN-1-wSc and Lifeact-NeonGreen. We also imaged a SNN-1-Venus strain. In N2 worms, Lifeact-NG was distributed in discrete puncta along the DA axon overlapping with the presynaptic marker SNN-1-wSc (Fig. 10a,b). We measured the average distance between the SNN-1-wSc peaks and the Lifeact-NG peaks. We observed this distance increased in phac-1(lf) compared with controls (Fig. 10c; p = 0.0337), suggesting ectopic F-actin structures occur away from the presynaptic terminals in phac-1(lf). The axonal and peak fluorescence of Lifeact-NG was reduced in *phac-1(lf)* mutants (axonal fluorescence: Fig. 10*d*, p = 0.0316; peak fluorescence: Fig. 10*e*, p = 0.0135). The peak density of Lifeact-NG remained unchanged in both mutants (Fig. 10*f*; phac-1(lf), p = 0.7863; phac-1(gf), p = 0.8225). We hypothesize that ectopic F-actin structures may lead to increased capture of DCVs away from the presynaptic terminals in phac-1(lf), as observed by EM (Fig. 9i).

In *phac-1*(*lf*) mutants, the axonal and the peak fluorescence of SNN-1-Venus were weakly reduced (axonal fluorescence: Fig. 10g, p = 0.0001; peak fluorescence: Fig. 10h, p = 0.0027), while the peak density was increased (Fig. 10i; p = 0.0003). The same quantifications were done for SNN-1-wSc. Although it did not reach significance, the same trends for reduced axonal SNN-1-wSc were observed in *phac-1*(*lf*) (Fig. 10j-l; axonal fluorescence: Fig. 10j, p = 0.1308; peak fluorescence: Fig. 10k, p = 0.1577). Together, these results suggest SNN-1 spreads away from the presynaptic terminals in *phac-1*(*lf*).

phac-1 and snn-1 act together to regulate the NMJ

Given that the SNN-1 level and distribution were affected in phac-1(lf) and that snn-1(ulb14) was identified alongside phac-1(ulb03) as suppressors of the FLP-18 overexpression phenotype, we explored a potential genetic interaction between phac-1 and snn-1. A null allele of snn-1(tm2557) was previously described (Yu et al., 2021). Upon introduction of the *snn-1(tm2557)* mutation into *phac-1(gf)* mutants, we noted a significant reduction in the aldicarb resistance (Fig. 11a; phac-1(gf) vs phac-1(gf); snn-1(tm2557), q < 0.0001). These results fit a model in which synapsin/snn-1 mediates the aldicarb resistance of phac-1(gf). Phosphoregulation of serine 9 in SNN-1 controls the capture of DCV by presynaptic terminals (Yu et al., 2021). Independently, serine 9 of synapsin I appeared among the candidate peptide substrates of the PP1-PHACTR1 holophosphatase identified by a SILAC approach in mouse primary neurons (Fedoryshchak et al., 2020). To directly analyze the phosphorylation state of serine 9 SNN-1, we designed antibodies against a 13-amino acid peptide that included the phosphorylated Ser9 of SNN-1. The specificity of the phosphoantibody was confirmed in snn-1(tm2557) and in the phosphodeficient strain snn-1(S9A) (Yu et al., 2021). Analysis of SNN-1 by Western blot revealed that phosphorylation of Ser9 was increased in phac-1(lf) (Fig. 11b; p = 0.0409). If the dephosphorylation of SNN-1 Ser9 mediates the aldicarb resistance of phac-1(gf), a phosphodeficient allele of snn-1(S9A) should mimic the aldicarb resistance of phac-1(gf) and suppress the aldicarb hypersensitivity of phac-1(lf). Accordingly, the snn-1(S9A) allele replicated the aldicarb resistance of phac-1(gf) (Fig. 11c; snn-1(S9A) vs N2, q = 0.0116; snn-1(S9A) vs phac-1(2R/A), q = 0.2607). Also *snn-1(S9A)* reduced the aldicarb hypersensitivity of phac-1(lf) (Fig. 11c; phac-1(lf) vs snn-1(S9A); phac-1(lf), q = 0.0012; snn-1(S9A); phac-1(lf) vs N2, q = 0.2853).

Discussion

Bioamines and neuropeptides modulate neurotransmitter release at NMJs through synaptic or extrasynaptic GPCR signaling (Nurrish et al., 1999; Hu et al., 2011, 2015; Taghert and Nitabach, 2012). In C. elegans, activity-induced transcription of neuropeptides, such as FLP-18, helps to fine-tune the excitatory/inhibitory (E/I) balance of motor circuits (Stawicki et al., 2013; Hums et al., 2016; Ji et al., 2023). Specifically, overexpression of FLP-18 perturbs this E/I balance, leading to uncoordinated locomotion (Stawicki et al., 2013; Bhardwaj et al., 2018; Florman and Alkema, 2022). We found that disrupting the sole C. elegans orthologs of PHACTRs and synapsins, namely, phac-1 and snn-1, suppressed the FLP-18-induced defects. This suggests these genes are crucial for maintaining E/I balance in the motor circuit of C. elegans in response to neuropeptide signaling. Interestingly, variants of both PHACTR1 and synapsin I can cause human epilepsy, underscoring potentially conserved

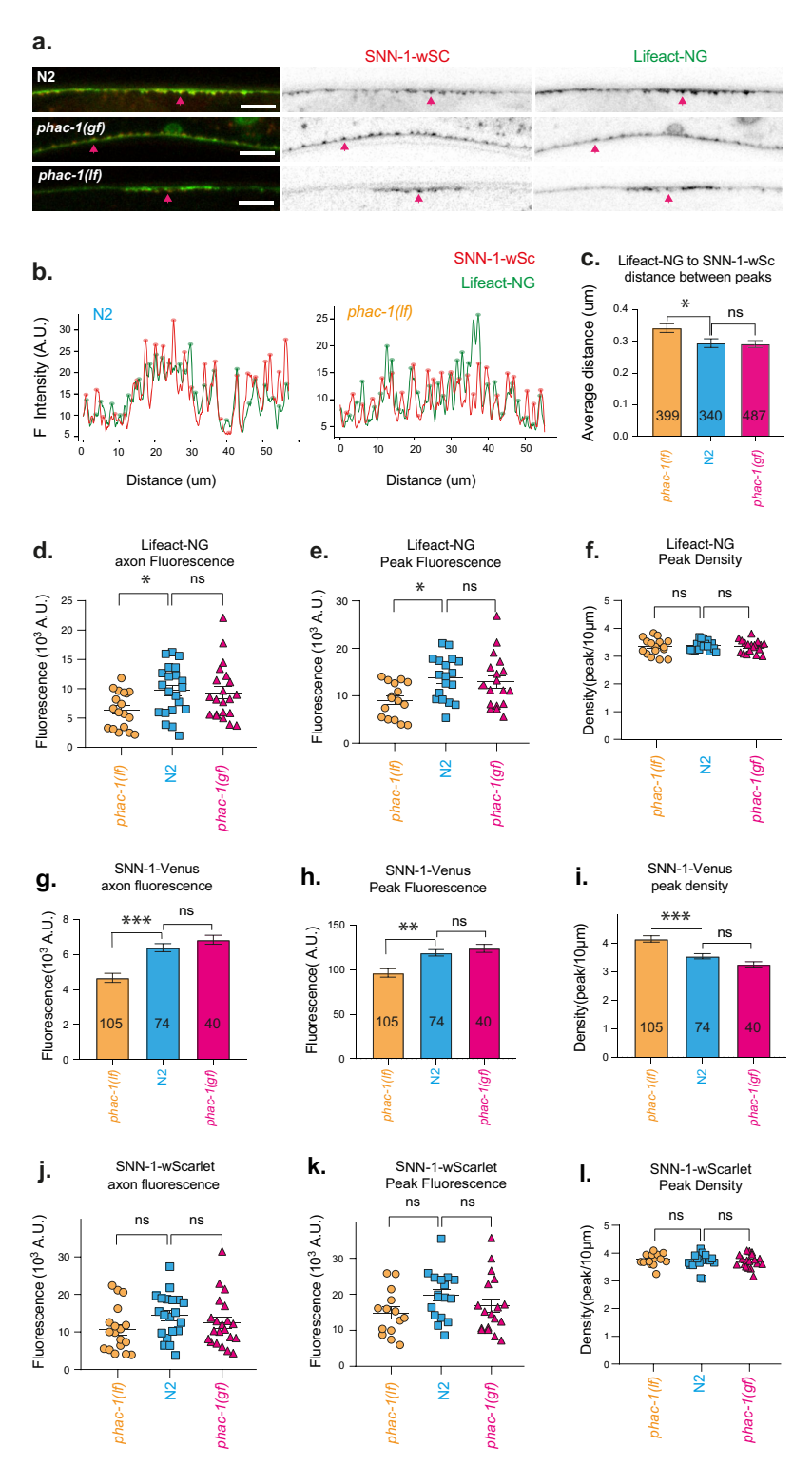


Figure 10. The distribution of SNN-1 and F-actin is altered in phac-1(lf) mutants. a, Representative distribution of coexpressed SNN-wScarlet (red) and of Lifeact-NG (green) along a DA axon. Bright SNN-1-wScarlet puncta correspond to presynaptic SV clusters (red arrowhead), while Lifeact-NG corresponds to labeled F-actin. Scale bar, 10 μ m. b, Fluorescence distribution of Lifeact-NG and SNN-1-wSc, along the DNC in N2 (left) and in phac-1(lf) (right). In phac-1(lf), the Lifeact-NG peaks appear slightly away from the SNN-1-wSc-marked SV clusters. c, The average distance between SNN-1-wScarlet and Lifeact-NG peaks is significantly increased in phac-1(lf) compared with N2, suggesting ectopic F-actin structures. d-f, The fluorescence of Lifeact-NG along the DA axon was analyzed. The total Lifeact-NG fluorescence along the DA axon (d) and the Lifeact-NG peak fluorescence (e) are reduced in phac-1(lf) mutants. The peak density of Lifeact-NG (f) is not affected in phac-1 mutants. g-i, The fluorescence of SNN-1-Venus along the DA axon was analyzed. The total fluorescence along the DA axon (g) and the peak fluorescence (h) of SNN-1-Venus are significantly reduced in phac-1(lf) compared with N2; the peak density (f) is increased in phac-1(lf). More parameters on SNN-1-Venus are available in Extended Data 2. j-l, The fluorescence of SNN-1-WSc along the DA axon (g), the peak fluorescence (k), and the peak density (l) of SNN-1-wSc were not significantly altered in phac-1 mutants. Data are plotted as the mean \pm SEM. One-way ANOVA and Tukey's (10c, e-l) or Dunn's (10d, j-l) for multiple comparisons. ns, p > 0.05; **, $p \le 0.05$; **, $p \le 0.05$; **, $p \le 0.01$; ***, $p \le 0.01$; ****, $p \le 0.001$.

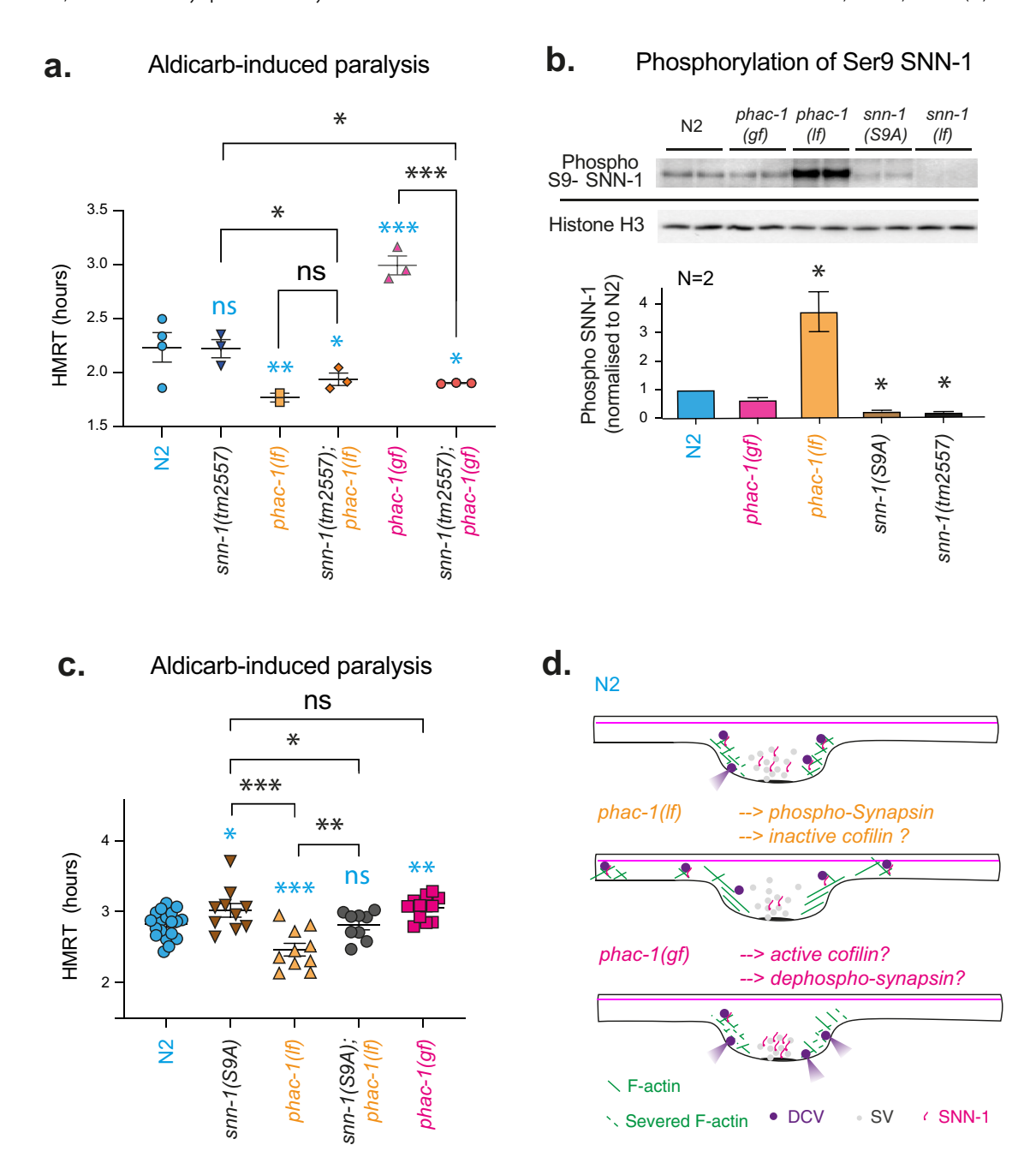


Figure 11. phac-1 and snn-1 act together to regulate the NMJ. a, The aldicarb assay (at 0.5 mM) is used for the epistatic analysis of the interactions of phac-1(lf) and (gf) alleles with snn-1(tm2557). The intermediate aldicarb responses of the double mutants phac-1(lf); snn-1(tm2557) or phac-1(gf); snn-1(tm2557) compared with the respective phac-1 alleles suggests that snn-1 mediates the aldicarb phenotype of phac-1 mutants. b, Representative Western blot of proteins extracted from C. elegans strains as indicated. The membrane was cut, and (phosphoS9)-SNN-1 was detected by an antibody recognizing an N-terminal phosphorylated peptide while an antibody recognizing Histone H3 provides a loading control, and the two blots are separated by a line. The specificity of the anti-SNNwas -1 antibody demonstrated in snn-1(tm2557) null mutants and in the phosphodeficient snn-1(S9A) animals. The density of the phospho-S9-SNN-1 bands were normalized to the density of H3 bands and to N2 values. Phosphorylation is significantly increased in phac-1(lf), weakly decreased in phac-1(gf), and significantly decreased in snn-1(null) compared with N2. c, Epistasis of phac-1(lf) with the synapsin-phosphodeficient allele snn-1(S9A) is analyzed using the aldicarb assay (at 0.5 mM). snn-1(S9A) phenocopies the aldicarb resistance of phac-1(gf). The intermediate aldicarb response of phac-1(lf), snn-1(S9A) double mutants compared with phac-1(lf) and N2 suggests that snn-1 is not the only effector of phac-1. d, Model of PHAC-1 signaling impact on DCV dynamics. PHAC-1 signaling modulates the remodeling of F-actin and SNN-1, which in turn affects the capture and release DCVs at presynaptic sites. In phac-1(gf), dephosphorylated SNN-1 and dynamic F-actin promoted by cofilin severing may facilitate the presynaptic capture of DCVs and their access to membrane for release, respectively. In the absence of SNN-1, DCV capture is impaired, thereby correcting the aldicarb resistance phen

mechanisms for controlling the E/I imbalance (Fassio et al., 2011; Hamada et al., 2018; Parenti et al., 2022).

We observe a partial rescue of the *phac-1(lf)* phenotype through the neuronal expression of human PHACTR1. This result suggests that the regulation of the PHACTR1/PHAC-1 holophosphatase, along with functions and substrates, is conserved in neurons. Using the aldicarb assay, we characterized the E/I balance in the motor circuit in the absence of *phac-1* or in point mutants mimicking the DEE70 variants in *phac-1*. A previous publication combining knockdown of PHACTR1 with the expression of rescue constructs in the embryonic mouse brain concluded that four DEE70 variants had dominant-negative effects: *N479I*, *L500P*, *I518N*, and *R521C* (Hamada et al., 2018). In contrast, we show that mutations mimicking *L500P*, *L519R*, and *R521C* in PHAC-1 cause a gf phenotype in *C. elegans*, resulting in faster locomotion and aldicarb resistance—the opposite phenotypes of *phac-1(lf)*.

PHACTRs are thought to cycle between an active holophosphatase state when bound to PP1 and an inactive, G-actin bound state (Mouilleron et al., 2012; Wiezlak et al., 2012; Huet et al., 2013). Constitutive holoenzyme activity promotes aldicarb resistance: fusing PP1 to PHAC-1 and reducing G-actin binding to phac-1 or DEE70 variants all cause aldicarb resistance. The holoenzyme-induced aldicarb resistance entirely depends on holoenzyme activity: point mutations reducing PP1 activity or PP1 binding to PHAC-1 suppress the effects of PHAC-1 signaling. The fact that all DEE70 variants replace highly conserved amino acids within RPEL motifs involved in G-actin binding suggests DEE70 variants reduce G-actin binding to PHAC-1, favoring PP1 binding and the active state of the PP1-PHAC-1 holophosphatase (Fig. 5a). This conclusion contrasts with the dominantnegative effects of DEE70 observed in Hamada et al. (2018), but confirms the model of Mouilleron et al. (2012), Wiezlak et al. (2012), Huet et al. (2013), and Marakhonov et al. (2021).

Given that G-actin regulates PHAC-1/PP1 activity physiologically, PHAC-1 signaling should vary as a consequence of actin polymerization at synapses that occur during SV endocytosis, recycling, and trafficking (Shupliakov et al., 2002; Sankaranarayanan et al., 2003; Bleckert et al., 2012; Ganguly et al., 2015; Soykan et al., 2017; Chenouard et al., 2020). Our results confirm the pathogenicity of DEE70 missense variants in C. elegans, providing evidence of its dominant positive effects and determining one potential mode of action for DEE70 in neurons: constitutive PHAC-1 signaling disrupts the proper regulation of presynaptic signaling. The substrates of the PHAC-1/PP1 holophosphatase are yet unknown. Our epistasis data suggest that phac-1(gf) regulates NMJ function upstream of snn-1, and we demonstrate that PHAC-1 regulates the Ser9 phosphorylation of SNN-1 as well as the SNN-1 axonal levels. The phosphorylation state of synapsin/ SNN-1 regulates its presynaptic localization, its interactions with the F-actin cytoskeleton, and its interactions with SV and DCVs (Hosaka et al., 1999; Fornasiero et al., 2012; Yu et al., 2021). As the phosphodeficient allele snn-1(S9A) only partially suppresses the aldicarb-hypersensitive phenotype of phac-1(lf), additional effectors/substrates of PP1-PHAC-1 likely exist. The consensus motif previously established for PHACTR1 substrates does not match the motif surrounding the Ser9 residue in SNN-1 (Fedoryshchak et al., 2020). Therefore, it remains possible that SNN-1 is indirectly dephosphorylated by PP1-PHAC-1 signaling.

Regulation of presynaptic DCV capture and exocytosis properties allows neurons to adapt to conditions of increased hormonal demand in invertebrates as well as in mammals (Wong et al., 2012; Bulgari et al., 2014; Anbalagan et al., 2019;

Kirchner et al., 2023). Several observations support the role of PHAC-1 signaling in the control of presynaptic DCV capture and neuropeptide secretion. First, FLP-18-induced behavior was reduced in phac-1(lf). Second, we observed increased neuropeptide secretion from DA cholinergic axons of phac-1(gf) animals. Third, more DCVs accumulate away from the presynaptic terminal in *phac-1(lf)*, and FRAP experiments show that 40% of DCVs in the *phac-1(lf)* axon are not exchanged compared with 30% in N2. Therefore, PHAC-1 signaling appears to regulate the presynaptic capture of DCV and their exocytosis. The differential regulation of F-actin organization and SNN-1 phosphorylation state by PHAC-1 suggests a model that differentially affects DCV capture and release in phac-1(lf) and phac-1(gf) mutants (Fig. 11d). In phac-1(lf), ectopic F-actin may trap DCVs away from presynaptic terminals. Poorly dynamic F-actin can form ectopically in the absence of cofilin activation by PHACTR signaling (Wiezlak et al., 2012; Huet et al., 2013; Fedoryshchak et al., 2020). In addition, hyperphosphorylated SNN-1 can prevent presynaptic DCV capture. In phac-1(gf), highly dynamic F-actin and dephosphorylated SNN-1 may facilitate presynaptic capture of DCVs and their access to the plasma membrane for exocytosis. Although DCVs are found in dendrites, axons, and presynaptic terminals, they are released differently in each subcompartment (van de Bospoort et al., 2012; Farina et al., 2015; Persoon et al., 2018). For example, DCVs trapped further away from the presynaptic calcium channels and exocytic machinery in *phac-1(lf)* are likely to be less susceptible to release.

Mechanistically, how E/I balance at NMJs is regulated by neuropeptide signaling in *phac-1* mutants remain to be determined. We show that PHAC-1 signaling modifies the *C. elegans* locomotion and the aldicarb-induced paralysis rate, impacts cholinergic NMJ ultrastructure, and affects SNB-1-pHluorin distribution, together suggesting an effect on SV recycling at cholinergic NMJs. However, the electrophysiological recordings did not reveal any differences in SV exocytosis at the NMJs of *phac-1* mutants. We suggest this discrepancy may be due to the recording conditions. The observed effects of PHAC-1 on peptidergic signaling may be mitigated during electrophysiological recordings done on immobilized worms with NMJs exposed to a bathing medium. As previously observed, these preparations lack proprioceptive feedback and favor the diffusion of peptidergic signals (Hu et al., 2011; Chen et al., 2024).

In summary, our results suggest that a G-actin-tuned PP1-PHAC-1 holoenzyme controls DCV distribution and neuropeptide release from the axon and presynaptic terminals, potentially through its regulation of the actin/synapsin cytoskeleton. Constitutive PHAC-1 signaling caused by DEE70 variants induces an oversecretion of neuropeptides. Disruption of the circuits' E/I balance by altered neuropeptide signaling might be a conserved mechanism of action of DEE70 to trigger seizures.

Inclusion and Diversity

We support inclusive, diverse, and equitable conduct of research.

References

Agostinho AS, et al. (2019) Dynorphin-based "release on demand" gene therapy for drug-resistant temporal lobe epilepsy. EMBO Mol Med 11:e9963. Allen PB, Greenfield AT, Svenningsson P, Haspeslagh DC, Greengard P (2004) Phactrs 1–4: a family of protein phosphatase 1 and actin regulatory proteins. Proc Natl Acad Sci U S A 101:7187–7192.

Anbalagan S, Blechman J, Gliksberg M, Gordon L, Rotkopf R, Dadosh T, Shimoni E, Levkowitz G (2019) Robo2 regulates synaptic oxytocin content by affecting actin dynamics. eLife 8:e45650.

- Bargmann CI (2012) Beyond the connectome: how neuromodulators shape neural circuits. Bioessays 34:458–465.
- Bhardwaj A, Thapliyal S, Dahiya Y, Babu K (2018) FLP-18 functions through the G-protein-coupled receptors NPR-1 and NPR-4 to modulate reversal length in *Caenorhabditis elegans*. J Neurosci 38:4641–4654.
- Bittins CM, Eichler TW, Hammer JA 3rd, Gerdes HH (2010) Dominantnegative myosin Va impairs retrograde but not anterograde axonal transport of large dense core vesicles. Cell Mol Neurobiol 30:369–379.
- Bleckert A, Photowala H, Alford S (2012) Dual pools of actin at presynaptic terminals. J Neurophysiol 107:3479–3492.
- Brenner S (1974) The genetics of *Caenorhabditis elegans*. Genetics 77:71–94. Bulgari D, Zhou C, Hewes RS, Deitcher DL, Levitan ES (2014) Vesicle capture, not delivery, scales up neuropeptide storage in neuroendocrine terminals. Proc Natl Acad Sci U S A 111:3597–3601.
- Cardona A, Saalfeld S, Schindelin J, Arganda-Carreras I, Preibisch S, Longair M, Tomancak P, Hartenstein V, Douglas RJ (2012) TrakEM2 software for neural circuit reconstruction. PLoS One 7:e38011.
- Cesca F, Baldelli P, Valtorta F, Benfenati F (2010) The synapsins: key actors of synapse function and plasticity. Prog Neurobiol 91:313–348.
- Chen L, Su P, Wang Y, Liu Y, Chen LM, Gao S (2024) CKR-1 orchestrates two motor states from a single motoneuron in *C. elegans*. iScience 27:109390.
- Chenouard N, Xuan F, Tsien RW (2020) Synaptic vesicle traffic is supported by transient actin filaments and regulated by PKA and NO. Nat Commun 11:5318
- Ch'ng Q, Sieburth D, Kaplan JM (2008) Profiling synaptic proteins identifies regulators of insulin secretion and lifespan. PLoS Genet 4:e1000283.
- Cohen M, Reale V, Olofsson B, Knights A, Evans P, de Bono M (2009) Coordinated regulation of foraging and metabolism in *C. elegans* by RFamide neuropeptide signaling. Cell Metab 9:375–385.
- Farina M, van de Bospoort R, He E, Persoon CM, van Weering JR, Broeke JH, Verhage M, Toonen RF (2015) CAPS-1 promotes fusion competence of stationary dense-core vesicles in presynaptic terminals of mammalian neurons. eLife 4:e05438.
- Fassio A, Raimondi A, Lignani G, Benfenati F, Baldelli P (2011) Synapsins: from synapse to network hyperexcitability and epilepsy. Semin Cell Dev Biol 22:408–415.
- Fedoryshchak RO, et al. (2020) Molecular basis for substrate specificity of the Phactr1/PP1 phosphatase holoenzyme. eLife 9:e61509.
- Florman JT, Alkema MJ (2022) Co-transmission of neuropeptides and monoamines choreograph the *C. elegans* escape response. PLoS Genet 18: e1010091.
- Fornasiero EF, Raimondi A, Guarnieri FC, Orlando M, Fesce R, Benfenati F, Valtorta F (2012) Synapsins contribute to the dynamic spatial organization of synaptic vesicles in an activity-dependent manner. J Neurosci 32:12214–12227.
- Ganguly A, Tang Y, Wang L, Ladt K, Loi J, Dargent B, Leterrier C, Roy S (2015) A dynamic formin-dependent deep F-actin network in axons. J Cell Biol 210:401–417.
- Ghanta KS, Mello CC (2020) Melting dsDNA donor molecules greatly improves precision genome editing in *Caenorhabditis elegans*. Genetics 216:643–650.
- Giakoumakis NN, Rapsomaniki MA, Lygerou Z (2017) Analysis of protein kinetics using fluorescence recovery after photobleaching (FRAP). Methods Mol Biol 1563:243–267.
- Guerrini R, Conti V, Mantegazza M, Balestrini S, Galanopoulou AS, Benfenati F (2023) Developmental and epileptic encephalopathies: from genetic heterogeneity to phenotypic continuum. Physiol Rev 103:433–513.
- Hamada N, et al. (2018) De novo PHACTR1 mutations in West syndrome and their pathophysiological effects. Brain 141:3098–3114.
- Haque R, Shamsuzzama, Kumar L, Sharma T, Fatima S, Jadiya P, Siddiqi MI, Nazir A (2020) Human insulin modulates alpha-synuclein aggregation via DAF-2/DAF-16 signalling pathway by antagonising DAF-2 receptor in C. elegans model of Parkinson's disease. Oncotarget 11:634–649.
- Hornberg H, Perez-Garci E, Schreiner D, Hatstatt-Burkle L, Magara F, Baudouin S, Matter A, Nacro K, Pecho-Vrieseling E, Scheiffele P (2020) Rescue of oxytocin response and social behaviour in a mouse model of autism. Nature 584:252–256.
- Hosaka M, Hammer RE, Sudhof TC (1999) A phospho-switch controls the dynamic association of synapsins with synaptic vesicles. Neuron 24: 377–387
- Hu Z, Pym EC, Babu K, Vashlishan Murray AB, Kaplan JM (2011) A neuropeptide-mediated stretch response links muscle contraction to changes in neurotransmitter release. Neuron 71:92–102.

- Hu Z, Vashlishan-Murray AB, Kaplan JM (2015) NLP-12 engages different UNC-13 proteins to potentiate tonic and evoked release. J Neurosci 35: 1038–1042.
- Huet G, Rajakyla EK, Viita T, Skarp KP, Crivaro M, Dopie J, Vartiainen MK (2013) Actin-regulated feedback loop based on Phactr4, PP1 and cofilin maintains the actin monomer pool. J Cell Sci 126:497–507.
- Hums I, Riedl J, Mende F, Kato S, Kaplan HS, Latham R, Sonntag M, Traunmuller L, Zimmer M (2016) Regulation of two motor patterns enables the gradual adjustment of locomotion strategy in *Caenorhabditis ele*gans. eLife 5:e14116.
- Javer A, Ripoll-Sanchez L, Brown AEX (2018) Powerful and interpretable behavioural features for quantitative phenotyping of *Caenorhabditis ele*gans. Philos Trans R Soc Lond B Biol Sci 373:20170375.
- Ji H, Fouad AD, Li Z, Ruba A, Fang-Yen C (2023) A proprioceptive feedback circuit drives Caenorhabditis elegans locomotor adaptation through dopamine signaling. Proc Natl Acad Sci U S A 120:e2219341120.
- Kavalali ET, Jorgensen EM (2014) Visualizing presynaptic function. Nat Neurosci 17:10–16.
- Kim TH, Goodman J, Anderson KV, Niswander L (2007) Phactr4 regulates neural tube and optic fissure closure by controlling PP1-, Rb-, and E2F1-regulated cell-cycle progression. Dev Cell 13:87–102.
- Kirchner MK, Althammer F, Donaldson KJ, Cox DN, Stern JE (2023) Changes in neuropeptide large dense core vesicle trafficking dynamics contribute to adaptive responses to a systemic homeostatic challenge. iScience 26:108243.
- Lambert TJ (2019) FPbase: a community-editable fluorescent protein database. Nat Methods 16:277–278.
- Laurent P, Ch'ng Q, Jospin M, Chen C, Lorenzo R, de Bono M (2018)
 Genetic dissection of neuropeptide cell biology at high and low
 activity in a defined sensory neuron. Proc Natl Acad Sci U S A 115:
 E6890–E6899.
- Li L, et al. (2021) A novel dual Ca2+ sensor system regulates Ca2+-dependent neurotransmitter release. J Cell Biol 220:e202008121.
- Liu H, Li L, Krout M, Sheoran S, Zhao Q, Chen J, Liu H, Richmond JE, Hu Z (2021) Protocols for electrophysiological recordings and electron microscopy at C. elegans neuromuscular junction. STAR Protoc 2:100749.
- Mahoney TR, Luo S, Nonet ML (2006) Analysis of synaptic transmission in Caenorhabditis elegans using an aldicarb-sensitivity assay. Nat Protoc 1: 1772–1777
- Marakhonov AV, et al. (2021) Mutation in PHACTR1 associated with multifocal epilepsy with infantile spasms and hypsarrhythmia. Clin Genet 99:673–683.
- Marder E (2012) Neuromodulation of neuronal circuits: back to the future. Neuron 76:1–11.
- Martin JA, Hu Z, Fenz KM, Fernandez J, Dittman JS (2011) Complexin has opposite effects on two modes of synaptic vesicle fusion. Curr Biol 21: 97–105
- McCulloch KA, Zhou K, Jin Y (2020) Neuronal transcriptome analyses reveal novel neuropeptide modulators of excitation and inhibition imbalance in *C. elegans.* PLoS One 15:e0233991.
- McTague A, Howell KB, Cross JH, Kurian MA, Scheffer IE (2016) The genetic landscape of the epileptic encephalopathies of infancy and childhood. Lancet Neurol 15:304–316.
- Mello CC, Kramer JM, Stinchcomb D, Ambros V (1991) Efficient gene transfer in *C. elegans*: extrachromosomal maintenance and integration of transforming sequences. EMBO J 10:3959–3970.
- Melzer S, et al. (2021) Bombesin-like peptide recruits disinhibitory cortical circuits and enhances fear memories. Cell 184:5622–5634.e5.
- Minevich G, Park DS, Blankenberg D, Poole RJ, Hobert O (2012) CloudMap: a cloud-based pipeline for analysis of mutant genome sequences. Genetics 192:1249–1269.
- Mouilleron S, Wiezlak M, O'Reilly N, Treisman R, McDonald NQ (2012) Structures of the Phactr1 RPEL domain and RPEL motif complexes with G-actin reveal the molecular basis for actin binding cooperativity. Structure 20:1960–1970.
- Nelson SB, Valakh V (2015) Excitatory/inhibitory balance and circuit homeostasis in autism spectrum disorders. Neuron 87:684–698.
- Nurrish S, Segalat L, Kaplan JM (1999) Serotonin inhibition of synaptic transmission: Galpha(0) decreases the abundance of UNC-13 at release sites. Neuron 24:231–242.
- Parenti I, et al. (2022) The different clinical facets of SYN1-related neurodevelopmental disorders. Front Cell Dev Biol 10:1019715.

- Persoon CM, Moro A, Nassal JP, Farina M, Broeke JH, Arora S, Dominguez N, van Weering JR, Toonen RF, Verhage M (2018) Pool size estimations for dense-core vesicles in mammalian CNS neurons. EMBO J 37:e99672.
- Richmond JE, Davis WS, Jorgensen EM (1999) UNC-13 is required for synaptic vesicle fusion in *C. elegans*. Nat Neurosci 2:959–964.
- Sankaranarayanan S, Atluri PP, Ryan TA (2003) Actin has a molecular scaffolding, not propulsive, role in presynaptic function. Nat Neurosci 6:127–135.
- Schenk C, Bringmann H, Hyman AA, Cowan CR (2010) Cortical domain correction repositions the polarity boundary to match the cytokinesis furrow in *C. elegans* embryos. Development 137:1743–1753.
- Schindelin J, et al. (2012) Fiji: an open-source platform for biological-image analysis. Nat Methods 9:676–682.
- Senti G, Swoboda P (2008) Distinct isoforms of the RFX transcription factor DAF-19 regulate ciliogenesis and maintenance of synaptic activity. Mol Biol Cell 19:5517–5528.
- Shupliakov O, Bloom O, Gustafsson JS, Kjaerulff O, Low P, Tomilin N, Pieribone VA, Greengard P, Brodin L (2002) Impaired recycling of synaptic vesicles after acute perturbation of the presynaptic actin cytoskeleton. Proc Natl Acad Sci U S A 99:14476–14481.
- Sieburth D, et al. (2005) Systematic analysis of genes required for synapse structure and function. Nature 436:510–517.
- Soykan T, Kaempf N, Sakaba T, Vollweiter D, Goerdeler F, Puchkov D, Kononenko NL, Haucke V (2017) Synaptic vesicle endocytosis occurs on multiple timescales and is mediated by formin-dependent actin assembly. Neuron 93:854–866.e4.
- Stawicki TM, Takayanagi-Kiya S, Zhou K, Jin Y (2013) Neuropeptides function in a homeostatic manner to modulate excitation-inhibition imbalance in *C. elegans*. PLoS Genet 9:e1003472.
- Sumakovic M, Hegermann J, Luo L, Husson SJ, Schwarze K, Olendrowitz C, Schoofs L, Richmond J, Eimer S (2009) UNC-108/RAB-2 and its effector RIC-19 are involved in dense core vesicle maturation in *Caenorhabditis* elegans. J Cell Biol 186:897–914.
- Taghert PH, Nitabach MN (2012) Peptide neuromodulation in invertebrate model systems. Neuron 76:82–97.

- van de Bospoort R, Farina M, Schmitz SK, de Jong A, de Wit H, Verhage M, Toonen RF (2012) Munc13 controls the location and efficiency of densecore vesicle release in neurons. J Cell Biol 199:883–891.
- Watanabe S, Davis MW, Kusick GF, Iwasa J, Jorgensen EM (2020) SynapsEM: computer-assisted synapse morphometry. Front Synaptic Neurosci 12: 584549.
- Weimer RM, Gracheva EO, Meyrignac O, Miller KG, Richmond JE, Bessereau JL (2006) UNC-13 and UNC-10/rim localize synaptic vesicles to specific membrane domains. J Neurosci 26:8040–8047.
- White JG, Southgate E, Thomson JN, Brenner S (1976) The structure of the ventral nerve cord of *Caenorhabditis elegans*. Philos Trans R Soc Lond B Biol Sci 275:327–348.
- White JG, Southgate E, Thomson JN, Brenner S (1986) The structure of the nervous system of the nematode *Caenorhabditis elegans*. Philos Trans R Soc Lond B Biol Sci 314:1–340.
- Wiezlak M, Diring J, Abella J, Mouilleron S, Way M, McDonald NQ, Treisman R (2012) G-actin regulates the shuttling and PP1 binding of the RPEL protein Phactr1 to control actomyosin assembly. J Cell Sci 125:5860–5872.
- Wong MY, Zhou C, Shakiryanova D, Lloyd TE, Deitcher DL, Levitan ES (2012) Neuropeptide delivery to synapses by long-range vesicle circulation and sporadic capture. Cell 148:1029–1038.
- Yu SC, Janosi B, Liewald JF, Wabnig S, Gottschalk A (2018) Endophilin A and B join forces with clathrin to mediate synaptic vesicle recycling in *Caenorhabditis elegans*. Front Mol Neurosci 11:196.
- Yu SC, Liewald JF, Shao J, Steuer Costa W, Gottschalk A (2021) Synapsin is required for dense core vesicle capture and cAMP-dependent neuropeptide release. J Neurosci 41:4187–4201.
- Zhang L, Wang Y, Dong Y, Pant A, Liu Y, Masserman L, Xu Y, McLaughlin RN Jr, Bai J (2022) The endophilin curvature-sensitive motif requires electrostatic guidance to recycle synaptic vesicles in vivo. Dev Cell 57: 750–766.e5.
- Zhang J, Zhang Z, Brew K, Lee EY (1996) Mutational analysis of the catalytic subunit of muscle protein phosphatase-1. Biochemistry 35: 6276–6282.